

**A Numerical Study of  
Solid Oxide Iron–Air Battery:  
Thermodynamic Analysis and  
Heat and Mass Transfer Characteristics**

Hiroko Ohmori



# Contents

<b>Acknowledgement</b>	<b>v</b>
<b>1. Introduction</b>	<b>1</b>
1.1. Background .....	1
1.2. Outline of the thesis .....	6
References .....	7
<b>2. Outline of the SOIAB</b>	<b>13</b>
2.1. Reversible reactions during discharge/charge operations .....	13
2.2. Battery designs .....	17
References .....	20
<b>3. System round-trip efficiency of SOIAB</b>	<b>23</b>
3.1. Numerical modeling .....	23
3.1.1. Conditions and assumptions .....	23
3.1.2. System round-trip efficiency .....	26
3.1.3. Generation/absorption of thermal energy and heat transfer .....	28
3.1.3.1. Reaction heat .....	28
3.1.3.2. Losses in SOEC .....	29
3.1.3.3. Gas preheating .....	29

3.1.3.4. Heat inputs to system during charge and discharge processes .....	30
3.1.3.5. Heat inputs to system with thermal recirculation .....	30
3.2. Results and discussion .....	33
3.2.1. Energy budget of fundamental system without thermal recirculation .....	33
3.2.2. Energy flows in SOIAB system with thermal recirculation .....	37
3.2.3. Effects of heat exchanger effectiveness on round-trip efficiency .....	40
3.2.4. Effects of gas utilization factors on round-trip efficiency and efficient and uniform operation .....	42
3.2.5. Effects of current density on round-trip efficiency .....	45
3.3. Summary .....	47
References .....	49

## **4. 1-D numerical simulation of mass transfer effects on SOIAB      51**

4.1. Numerical procedure .....	51
4.1.1. Battery design and computational domain .....	51
4.1.2. Numerical modeling .....	53
4.1.2.1. Governing equation .....	53
4.1.2.2. Metal redox reaction model .....	54
4.1.2.3. Electrochemical model of the SOEC .....	55
4.1.2.4. Numerical procedure .....	56
4.1.2.5. Computational conditions .....	56
4.2. Results and discussion .....	58
4.2.1. Fundamental characteristics charge/discharge operations .....	58
4.2.2. Gas diffusion during operations .....	58

4.2.3. Evolution of redox reaction area .....	60
4.2.4. Effects of current density .....	64
4.2.5. Effects of amount of the redox metal .....	66
4.3. Summary .....	68
References .....	70

## **5. 2-D numerical simulation of heat and mass transfer effects on SOIAB 71**

5.1. Numerical procedure .....	71
5.1.1. Battery design and computational domain .....	71
5.1.2. Numerical modeling .....	73
5.1.2.1 1-D simulation models for air flow and SOEC .....	74
5.1.2.2 2-D simulation model in the container .....	75
5.1.2.3 Redox reaction model of metal .....	76
5.1.2.4 Reaction model at SOEC .....	78
5.1.2.5 Numerical procedure .....	80
5.1.2.6 Computational conditions .....	81
5.2. Results and discussion .....	84
5.2.1. Fundamental characteristics under discharge/charge operations .....	84
5.2.2. Heat transfer during discharge operation .....	86
5.2.3. Current density distribution of SOEC during discharge operation .....	89
5.2.4. Evolution of redox reaction area during discharge operation .....	91
5.2.5. Gas diffusion during discharge operation .....	96

5.2.6. Charge operation .....	99
5.2.7. Discharge/charge cycle operation .....	104
5.3. Summary .....	108
References .....	110
<b>6. Conclusions</b> .....	<b>111</b>
6.1. Conclusions .....	111
6.2. Suggestions for future works .....	114
<b>Nomenclature</b> .....	<b>115</b>

# Acknowledgement

It is my great pleasure to express my sincere appreciation to all people who supported me throughout my Ph.D work in the Thermal Engineering Laboratory of Kyoto University.

First of all, my heartfelt appreciation goes to Associate Professor Hiroshi Iwai of Kyoto University, whose invaluable guidance and suggestion helped me to learn the basics of research processes throughout my study.

I would also like to show my appreciation to Professor Hideo Yoshida of Kyoto University for his encouragement, generous assistance and suggestions, and Professor Koichi Eguchi and Professor Motofumi Suzuki of Kyoto University for their experienced suggestions.

I would also like to express my appreciation to Professor Tatsumi Ishihara of Kyushu University and Mr. Motohiro Nakanishi of Konica Minolta, Inc. who organized a project on this theme, Advanced Low Carbon Technology R&D program (ALCA) founded by Japan Science and Technology Agency (JST), and Mr. Nobuhisa Ishida of Konica Minolta, Inc. for his innovative ideas and advices. I would also like to thank Professor Kiyoshi Otsuka of Tokyo Institute of Technology, Professor Masahiro Kishida of Kyushu University and Professor Yoshinobu Fujishiro from National Institute of Advanced Industrial Science and Technology for their technical support and discussion. Thanks are expressed here to the members of the Thermal Engineering Laboratory, particularly to Mr. Kotaro Itakura, Assistant Professor Motohiro Saito,

Assistant Professor Masashi Kishimoto, Mr. Tetsushi Isomoto and Mr. Kota Miyoshi for their research collaborations and suggestions.

Finally, I would like to express my thanks to my family and friends for their constant support throughout my study.

# Chapter 1

## Introduction

### 1.1 Background

Development of a large-capacity energy-storage device is a key to realize an efficient smart grid system. It will enhance the capability of the smart grid to control and optimize the balance of power generation and consumption. It is also expected to function as a buffer for the fluctuation of power supply from the renewable energy sources [1.1-1.3]. Various types of rechargeable batteries are in use or under development today, in order to meet the requirement of the smart grid, that is, high rate capacity, high round-trip efficiency, long cycle life, and low life-cycle cost.

For example, Na-S battery and Li-ion battery stand out for their steady charge/discharge characteristics. Low energy density, short shelf life, and use of toxic materials are, however, the drawbacks that must be overcome before a wide commercialization [1.4]. Metal-air batteries also attract considerable attention as a rechargeable battery, owing to their large capacity due to the unnecessary of oxidizer storage at the cathode [1.5-1.9].

A solid oxide fuel cell (SOFC) is a device that directly converts the chemical energy of reactants into electricity. It has an advantage of high power generation efficiency even in systems with a relatively small capacity, compared with many other energy systems. Intensive research and development are underway with variety of possible applications such as portable systems [1.10, 1.11], residential cogeneration system [1.12-14], vehicle APUs [1.15] and power supply systems including hybrid system with gas turbines [1.16, 1.17].

Recently, much attention is also paid to its reverse reaction, electrolysis [1.18-20]. Steam is electrochemically decomposed into hydrogen and oxygen while consuming electric energy in this reaction. From the energy point of view, we can convert the input electric energy into the chemical energy of hydrogen through this reaction.

If a solid oxide electrochemical cell (SOEC) can operate in both the fuel cell and electrolysis modes, which is often called as a reversible SOEC, the SOEC can be used as energy storage systems [1.21-32]. When there is excess electricity, it is converted into the chemical energy of hydrogen and stored until it is converted again into electricity. Furthermore, hydrogen is not the only choice for the energy storage. For example, Wendel et al. reported an SOEC system to produce hydrocarbon fuel by methanation reaction of  $H_2/CO$  gained by electrolysis of steam/ $CO_2$  [1.21, 1.22]. Sun et al. presented a synthetic hydrocarbon fuel production using pressurized SOECs [1.22, 1.30]. In these examples the input energy is stored as chemical energy of generated gasses.

A new concept of storage battery was recently reported by Xu et al. [1.33]. This new concept battery consists of the reversible SOEC and the redox metal [1.34-44]. In this new battery, two reactions simultaneously proceed at two different locations. The

electrochemical reaction occurs at the SOEC and the redox reaction at the redox metal. In the discharge operation, hydrogen is consumed at the SOEC to generate electricity and steam. The generated steam is supplied for the metal oxidation where hydrogen is produced and it is supplied to the SOEC for further electricity generation. Then in the charge operation, steam is consumed by the electrolysis operation at the SOEC to generate hydrogen. The hydrogen is used to reduce the metal oxide and the produced steam is supplied to the SOEC for further electrolysis. Using iron as the redox metal, i.e., a solid oxide iron–air battery (SOIAB), the effectiveness of this concept was confirmed through laboratory-scale experiments [1.33, 1.37-41]. Unlike the gas phase storage explained in the previous paragraph, the overall reaction of this battery is the reduction and oxidation of metal. Therefore it can also be classified as a metal-air battery. One clear difference exists between the SOIAB and a conventional metal-air battery. Compared with conventional metal-air batteries, a major advantage of the SOIAB is the physical separation of the SOEC and the redox metal, which is enabled by the insertion of a gaseous hydrogen/steam mixture as an oxygen carrier between the two components. This can lead to cycle stability and easy system integration.

Because the concept of this battery is new and still in its early stage of development, the feasibility of the concept has intensively been studied from different aspects. Xu et al. [1.34] conducted a laboratory-scale experiment with a small tubular SOEC at 800 °C and examined the energy storage efficiency that was defined as a ratio of the output electricity against the input electricity. They successfully demonstrated the average energy storage efficiency of 92% over 20 stable charge/discharge cycles. Using an experimental setup similar to that of Xu et al., Zhao et al. [1.45, 1.46] performed cyclic durability tests. The battery was continuously cycled 100 times and a gradual

decline in performance was observed. Leonide et al. [1.47] reported the results of a long-term operation test utilizing an SOEC short stack at a constant temperature of 800 °C. They observed a decrease in the discharge capacity but nearly 40% of the storage metal remained active even after 10,000 cycles. Although the results of these experimental investigations are generally encouraging, further discussions are needed to clarify the feasibility of the SOIAB.

An SOIAB operates at elevated temperature around 500 - 800 °C. It also includes strong *exothermic* and/or *endothermic* reactions. Therefore, in addition to the energy storage efficiency (the ratio of electricity output to input), the system round-trip efficiency that considers not only the electric energy but the thermal energy input/output should be clarified. System-level analyses of SOIABs found in literature are, however, very few and its feasibility from the energy budget point of view is still unclear even for a fundamental system configuration.

Thermal management and the control of heat and mass transfer phenomena inside the SOIAB system is also important. While the entire SOIAB needs to be maintained at a sufficiently elevated temperature, a hot spot leads to a rapid degradation of the device. Sophisticated thermal management is essentially important to keep the spatial and temporal temperature within allowable limits. In addition, the redox metal is typically provided as porous body made of fine metal particles to ensure a large surface area. Its redox reaction is naturally accompanied with local volume change that inevitably affects the gas diffusion in the porous body. However, the heat and mass transfer inside the SOIAB has not been discussed in detail so far, although it has strong effects on performance, safety and durability of the battery.

The main objective of this study is to reveal the heat and mass transfer phenomena associated with safe and effective operations of solid oxide iron–air batteries to clarify the feasibility of SOIABs mainly from the point of view of thermal engineering and/or heat and mass transfer. System round-trip efficiency of a fundamental system configuration is discussed through system analyses while the detailed transport phenomena inside the SOIAB are numerically investigated.

## **1.2. Outline of the thesis**

Chapter 2 presents the outline of the SOIAB system including the reversible reactions at the SOEC and the redox metal during charge/discharge operations, and the classification of the system configurations.

Chapter 3 presents the study of system round-trip efficiency and energy flow of the system, based on a 0-D model under a quasi-steady-state assumption. The round-trip efficiency considering the electricity, chemical energy and thermal energy is investigated on models with/without thermal management.

Chapter 4 presents the study of 1-D analysis of mass transfer effects on the battery. Since the gas transfer between the SOEC and the redox metal is essential to the battery reactions, the distributions of the participating gas species in the system and their effects on the performance were focused with a simple model.

Chapter 5 presents the study of 2-D analysis of both heat and mass transfer effect. Because of heat generation/absorption during the operations, thermal management are dominant factor to the battery performance, in addition to gas transfer effects.

Chapter 6 summarizes the conclusions of this study and offers suggestions for future work.

## References

- [1.1] J. A. Turner, A realizable renewable energy future, *Science* 285 (1999) 687-689.
- [1.2] M. Roeb, H. Muller-Steinhagen, Concentrating on Solar Electricity and Fuels, *Science* 329 (2010) 773-774.
- [1.3] N. S. Lewis, Toward cost-effective solar energy use, *Science* 315 (2007) 798-801.
- [1.4] Z. Yang, J. Zhang, M. C. W. Kintner-Meyer, X. Lu, D. Choi, J. P. Lemmon, J. Liu, Electrochemical energy storage for green grid, *Chem. Rev.* 111 (2011) 3577-3613.
- [1.5] K. M. Abraham, Z. Jiang, A Polymer Electrolyte - Based Rechargeable Lithium/Oxygen Battery, *J. Electrochem. Soc.*, 143 (1996), 1-5.
- [1.6] A. K. Thapa, T. Ishihara, Mesoporous  $\alpha$ -MnO<sub>2</sub>/Pd catalyst air electrode for rechargeable lithium–air battery, *J. Power Sources*, 196 (2011), 7016-7020.
- [1.7] B. Dunn, H. Kamath, J. M. Tarascom, Electrical Energy Storage for the Grid: A Battery of Choices, *Science*, 334 (2011), 928-935.
- [1.8] S. J. Skinner, J. A. Kilner, Oxygen diffusion and surface exchange in La<sub>2-x</sub>Sr<sub>x</sub>NiO<sub>4+δ</sub>, *Solid State Ionics*, 135 (2000), 709-712.
- [1.9] N. Jayalakshmi, V. S. Muralidharan, Electrochemical behaviour of iron oxide electrodes in alkali solutions, *J. Power Sources*, 32 (1990), 277-286.
- [1.10] D. Pla, A. Sánchez-González, I. Garbayo, M. Salleras, A. Morata, A. Tarancón, Is it possible to design a portable power generator based on micro-solid oxide fuel cells? A finite volume analysis, *J. Power Sources*, 293 (2015) 264–273.

- [1.11] M. Reissig, J. Mathé, S. Planitzer, R. Vötter, J. Rechberger, Standalone Portable SOFC Power Generator for Autonomous Operation, *ECS Trans.* 68(1) (2015) 143-150.
- [1.12] R. Napoli, M. Gandiglio, A. Lanzini, M. Santarelli, Techno-economic analysis of PEMFC and SOFC micro-CHP fuel cell systems for the residential sector, *Energy and Buildings*, 103 (2015) 131–146.
- [1.13] S.J.G. Cooper, G.P. Hammond, M.C. McManus, A. Ramallo-Gonzalez, J.G. Rogers, Effect of operating conditions on performance of domestic heating systems with heat pumps and fuel cell micro-cogeneration, *Energy and Buildings*, 70 (2014) 52–60.
- [1.14] K.R. Ullah, R.K. Akikur, H.W. Ping, R. Saidur, S.A. Hajimolana, M.A. Hussain, An experimental investigation on a single tubular SOFC for renewable energy based cogeneration system, *Energy Conversion and Management*, 94 (2015) 139–149.
- [1.15] K. Kendall, J. Newton, M. Kendall, Microtubular SOFC (mSOFC) System in Truck APU Application, *ECS Trans.* 68(1) (2015) 187-192.
- [1.16] S. Wongchanapai, H. Iwai, M. Saito, H. Yoshida, Performance evaluation of a direct-biogas solid oxide fuel cell-micro gas turbine (SOFC-MGT) hybrid combined heat and power (CHP) system, *J. Power Sources* 223 (2013) 9-17.
- [1.17] High Efficiency SOFC Power Cycles With Indirect Natural Gas Reforming and CO<sub>2</sub> Capture, S. Campanari, M. Gazzani, *J. Fuel Cell Sci. Technol* 12 (2015) 021008-021017.
- [1.18] A. Hauch, S. D. Ebbesen, S. H. Jensen, M. Mogensen, Solid oxide electrolysis cells: Microstructure and degradation of the Ni/Yttria-stabilized Zirconia

- electrode, *J. Electrochem. Soc.* 155 (2008) B1184-B1193.
- [1.19] K. Eguchi, T. Hatagishi, H. Arai, Power generation and steam electrolysis characteristics of an electrochemical cell with a zirconia- or ceria-based electrolyte, *Solid State Ionics* 86-88 (1996) 1245-1249.
- [1.20] T. Ishihara, T. Kanno, Steam Electrolysis Using LaGaO<sub>3</sub> Based Perovskite Electrolyte for Recovery of Unused Heat Energy, *ISIJ Int.* 50 (2010) 1291-1295.
- [1.21] C. H. Wendela, P. Kazempoorb, R. J. Braun, A thermodynamic approach for selecting operating conditions in the design of reversible solid oxide cell energy systems, *J. Power Sources*, 301 (2016) 93-104.
- [1.22] C. H. Wendel, P. Kazempoor, R. J. Braun, Novel electrical energy storage system based on reversible solid oxide cells: System design and operating conditions, *J. Power Sources*, 276 (2015) 133-144.
- [1.22] S.H. Jensen, X. Sun, S.D. Ebbesen, R. Knibbe, M. Mogensen, A novel method for electrochemical electricity storage utilizing underground storage of methane and carbon dioxide, *Int. J. Hydrog. Energy* 35 (2010) 9544-9549.
- [1.23] T. Suzuki, T. Yamaguchi, K. Hamamoto, Y. Fujishiro, M. Awano, N. Sammes, A functional layer for direct use of hydrocarbon fuel in low temperature solid-oxide fuel cells, *Energy Environ. Sci.* 4 (2011) 940-943.
- [1.24] Z. Zhan, D. Han, T. Wu, X. Ye, S. Wang, T. Wen, S. Cho, S. A. Barnett, A solid oxide cell yielding high power density below 600 °C, *RSC Adv.* 2 (2012) 4075-4078.
- [1.25] C. Graves, S. D. Ebbesen, M. Mogensen, Co-electrolysis of CO<sub>2</sub> and H<sub>2</sub>O in solid oxide cells: Performance and durability, *Solid State Ionics*, 192 (2011)

398-403.

- [1.26] S.H. Jensen, C. Graves, M. Mogensen, C. Wendel, R. Braun, G. Hughes, Z. Gao, S.A. Barnett, Large-scale electricity storage utilizing reversible solid oxide cells combined with underground storage of CO<sub>2</sub> and CH<sub>4</sub>, *Energy & Environ. Sci.* 8 (2015) 2471-2479.
- [1.27] D.M. Bierschenk, J.R. Wilson, S.A. Barnett, High efficiency electrical energy storage using a methane–oxygen solid oxide cell, *Energy & Environ. Sci.* 4 (2011) 944-951.
- [1.28] C.H. Wendel, Z. Gao, S.A. Barnett, R.J. Braun, Modeling and experimental performance of an intermediate temperature reversible solid oxide cell for high-efficiency, distributed-scale electrical energy storage, *J. Power Sources* 283 (2015) 329-342.
- [1.29] W.L. Becker, R.J. Braun, M. Penev, M. Melaina, Production of Fischer–Tropsch liquid fuels from high temperature solid oxide co-electrolysis units, *Energy* 47 (2012) 99-115.
- [1.30] X. Sun, M. Chen, S.H. Jensen, S.D. Ebbesen, C. Graves, M. Mogensen, Thermodynamic analysis of synthetic hydrocarbon fuel production in pressurized solid oxide electrolysis cells, *Int. J. Hydrogen Energy* 37 (2012) 17101-17110.
- [1.31] J.E. O'Brien, M.G. McKellar, C.M. Stoots, J.S. Herring, G.L. Hawkes, Parametric study of large-scale production of syngas via high-temperature co-electrolysis, *Int. J. Hydrogen Energy* 34 (2009) 4216-4226.
- [1.32] C. Graves, S.D. Ebbesen, M. Mogensen, K.S. Lackner, Sustainable hydrocarbon fuels by recycling CO<sub>2</sub> and H<sub>2</sub>O with renewable or nuclear energy,

- Renew. Sustain. Energy, Rev. 15 (2011) 1-23.
- [1.33] N. Xu, X. Li, X. Zhao, J. B. Goodenough, K. Huang, A novel solid oxide redox flow battery for grid energy storage, *Energy Environ. Sci.* 4 (2011) 4942-4946.
- [1.34] X. Zhao, Y. Gong, X. Li, N. Xu, K. Huang, Performance of Solid Oxide Iron-Air Battery Operated at 550°C, *J. Electrochem. Soc.*, 160 (2013), A1241-A1247.
- [1.35] X. Zhao, N. Xu, X. Li, Y. Gong, K. Huang, Solid Oxide Iron-Air Rechargeable Battery-A New Energy Storage Mechanism, *ECS. Trans.*, 50 (2013), 115-123.
- [1.36] M. Guo, X. Zhao, R. E. White, K. Huang, A Multi-Physics Model for Solid Oxide Iron-Air Redox Flow Battery: Simulation of Discharge Behavior at High Current Density, *J. Electrochem. Soc.*, 160 (2013), A2085-A2092.
- [1.37] A. Inoishi, S. Ida, S. Uratani, T. Okano, T. Ishihara, High capacity of an Fe-air rechargeable battery using LaGaO<sub>3</sub>-based oxide ion conductor as an electrolyte, *Phys. Chem. Chem. Phys.*, 14 (2012), 12818-12822.
- [1.38] A. Inoishi, Y. W. Ju, S. Ida, T. Ishihara, Fe-air rechargeable battery using oxide ion conducting electrolyte of Y<sub>2</sub>O<sub>3</sub> stabilized ZrO<sub>2</sub>, *J. Power Sources*, 229 (2013), 12-15.
- [1.39] A. Inoishi, Y. Okamoto, Y. W. Ju, S. Ida, T. Ishihara, Oxidation rate of Fe and electrochemical performance of Fe-air solid oxide rechargeable battery using LaGaO<sub>3</sub> based oxide ion conductor, *RSC Adv.*, 3 (2013), 8820-8825.
- [1.40] H. Landes, R. Reichenbacher, Enhancement of Oxygen Transport in the Storage Electrode of a High Temperature Secondary Metal-Air Battery Based on an Oxygen Ion Conducting Electrolyte, *ECS. Trans.*, 50(25) (2013), 47-68.
- [1.41] W. Drenckhahn, H. Greiner, M. Kuhne, H. Landes, A. Leonide, K. Litzinger, C.

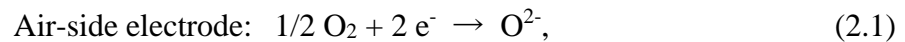
- Lu, C. Schuh, J. Shull, T. Soller, A Novel High Temperature Metal - Air Battery, ECS. Trans., 50(45) (2013), 125-135.
- [1.42] N. H. Menzler, A. Hospach, L. Niewolak, M. Bram, O. Tokariev, C. Berger, P. Orzessek, W. J. Quadackers, Q. Fang, H. P. Buchkremer, Power-To-Storage - The Use of an Anode-Supported Solid Oxide Fuel Cell as a High-Temperature Battery, ECS. Trans., 57 (2013), 255-267.
- [1.43] H. Ohmori, S. Uratani, H. Iwai, Numerical simulation of gas diffusion effects on charge/discharge characteristics of a solid oxide redox flow battery, J. Power Sources, 208 (2012), 383-390.
- [1.44] H. Iwai, H. Ohmori, K. Itakura, M. Saito, H. Yoshida, Numerical Prediction of System Efficiency of Solid Oxide Redox Flow Battery During Charge/Discharge Process, ECS Trans., 57 (2013), 2661-2670.
- [1.45] X. Zhao, N. Xu, X. Li, Y. Gong, K. Huang, Long term stability study of a solid oxide metal-air battery, ECS Trans. 45 (2013) 113-121.
- [1.46] X. Zhao, Y. Gong, X. Li, N. Xu, K. Huang, Cyclic durability of a solid oxide Fe-air redox battery operated at 650°C, J. Electrochem. Soc. 160 (2013) A1716-A1719.
- [1.47] A. Leonide, W. Drenckhahn, H. Greiner, Long term operation of rechargeable high temperature solid oxide batteries, Electrochem. Soc. 161 (2014) A1297-A1301.

# Chapter 2

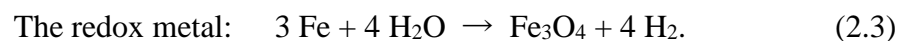
## Outline of the SOIAB

### 2.1. Reversible reactions during discharge/charge operations

Figure 2.1 schematically explains the concept of the battery with the reactions occurring at different positions. The battery consists of two main components, an SOEC and a redox metal facing the SOEC. The redox metal is typically provided in the form of fine particles to ensure large surface area. In his study, iron is assumed as the redox metal. In the discharge operation shown in Fig. 2.1 (a), the SOEC acts as a fuel cell generating electric power as follows;



The generated steam is transported to the redox metal by gas diffusion. It oxidizes the redox metal into a metal oxide as follows;



The generated hydrogen diffuses to the SOEC, and this cycle is repeated in the system.

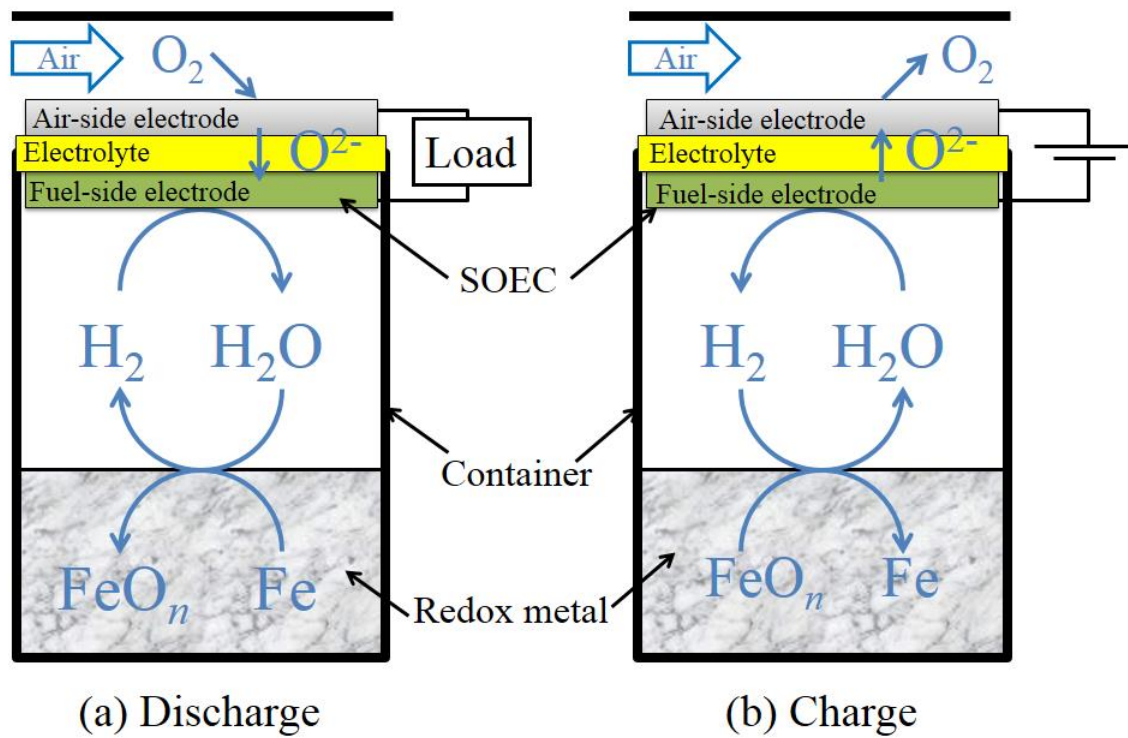
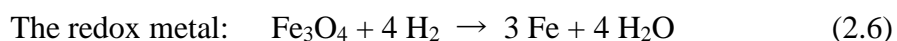
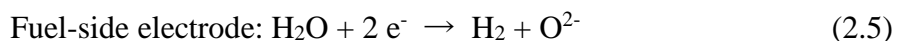
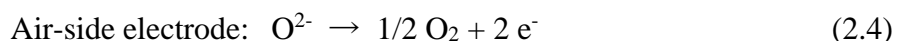


Figure 2.1. Reactions in (a) discharge operation and (b) charge operation.

When all (or a certain amount) of the redox metal is oxidized, the battery must be recharged.

Note that when iron is oxidized, the iron oxide can be wustite (FeO), magnetite (Fe<sub>3</sub>O<sub>4</sub>), or hematite (Fe<sub>2</sub>O<sub>3</sub>) depending on the temperature and oxygen partial pressure. According to the potential diagram of the Fe-O system [2.1-3], the dominant redox reaction in this study is between iron and magnetite because we assume a relatively low temperature of approximately 600 °C. The formation of magnetite was also confirmed in a preliminary experiment.

In the charge operation shown in Fig. 2.1 (b), all the above reactions proceed in the reverse direction. The SOEC acts as an electrolyzer and the metal oxide is reduced by hydrogen.



When all (or a certain amount) of the redox metal is reduced, the charge operation is completed and the system is ready for the next discharge. From the above reactions, the total reaction in the charge/discharge operation can be written as



Essentially, reaction (2.7) is similar to that of a typical iron–air battery. A major advantage of the SOIAB, however, is the physical separation of the electrochemical reaction (SOEC) from the redox reaction (the redox metal). This separation prevents structural damage that may occur from the change in volume of the redox metal associated with the redox reaction. It also gives us freedom to independently design the

power and capacity of the battery since the system output power depends on the total area of the SOEC electrode while the battery capacity is proportional to the amount of the redox metal.

The direction of the reversible metal redox reaction is governed by the composition of the gaseous hydrogen/steam mixture in the container. If the hydrogen partial pressure is greater than the equilibrium pressure of the redox reaction (Eqs. 2.3 and 2.6), the reduction is dominant, and vice versa. The hydrogen partial pressure is determined by hydrogen generation/absorption by the SOEC. As metal particles can easily be filled into spaces with various shapes, both tubular and planar SOECs are possible for this battery. Packed fine particles of the redox metal are used to ensure a large surface area. We treat the packed particles as a porous material in this study. When the redox metal is oxidized, its volume increases and the pore space in which the gas species diffuse is reduced. Therefore, a change in the state of the porous material affects the gas diffusion and redox reaction rate. With iron as the redox metal, the theoretical capacity density is 1280 Ah/kg-Fe, corresponding to the amount of hydrogen generated from iron.

## 2.2. Battery designs

Similarly to solid oxide fuel cells, many different cell designs and system configurations are possible for SOIABs [2.1-12]. The proposed system configurations reported in the literature can be classified into two groups.

In the first group, the SOEC and the redox metal are packed in a single package [2.2, 2.7, 2.11] as shown in Fig. 2.1. In the gap between the SOEC fuel electrode and the redox metal, the hydrogen/steam mixture naturally diffuses without any additional power input. That is, devices such as a blower for the hydrogen/steam mixture are not needed in this configuration and therefore the system is simple. Because the SOEC and the redox metal are physically close in this configuration, an operating temperature suitable for both electrochemical and redox reactions must be chosen. Considering the heat generation/absorption by the reactions, it can be considered that this configuration is more challenging from the viewpoint of thermal management.

In the other group, the SOEC and the redox metal are placed in different containers, and the two containers are connected via pipes to allow recirculation of the hydrogen/steam mixture [2.8, 2.12] as shown in Fig. 2.2. In this configuration, suitable operating temperatures for the SOEC and the redox metal can be separately selected. The system can be slightly complicated because a high-temperature blower is required for hydrogen/steam recirculation.

In this study, we first examine the system characteristics of an SOIAB and clarify the system round-trip efficiency that is one of the most fundamental information for discussion of its feasibility. The system analysis based on the components' 0-D models are possible for the configuration of the second group shown in Fig. 2.2. It is because

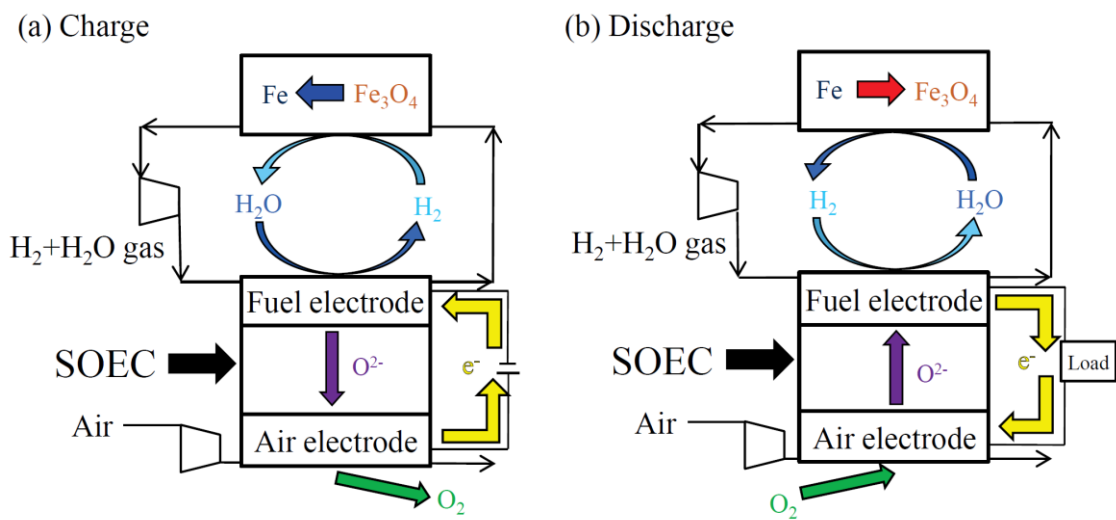


Figure 2.2. Schematic of the battery including the SOEC and the Fe box. Left: charge process, right: discharge process.

the components consisting of the system are separately allocated and the evaluation method of each component is available (Chapter 3). On the other hand, for the configuration of the first group shown in Fig. 2.1, the reactions of the SOEC and the redox iron strongly interact each other. The investigation of the heat and mass transfer phenomena inside the system becomes the main issue in this case. The 1-D mass transfer simulation (Chapter 4) and 2-D heat and mass transfer simulation (Chapter 5) are conducted.

The capacity of the battery can be adjusted by changing the amount of iron so that a system matches to an application. Because this is a battery operating at elevated temperature, we expect the system development starts with relatively small scale and will expand to larger systems, similar to SOFCs. We, therefore, assume a small system of 5-kWh capacity in this study. This is similar to a mid-range home-use battery system commercially available in Japan as of 2015

## References

- [2.1] X. Zhao, N. Xu, X. Li, Y. Gong, K. Huang, Solid Oxide Iron-Air Rechargeable Battery-A New Energy Storage Mechanism, *ECS. Trans.*, 50 (2013), 115-123.
- [2.2] A. Inoishi, Y. W. Ju, S. Ida, T. Ishihara, Fe-air rechargeable battery using oxide ion conducting electrolyte of Y<sub>2</sub>O<sub>3</sub> stabilized ZrO<sub>2</sub>, *J. Power Sources*, 229 (2013), 12-15.
- [2.3] A. Inoishi, Y. Okamoto, Y. W. Ju, S. Ida, T. Ishihara, Oxidation rate of Fe and electrochemical performance of Fe-air solid oxide rechargeable battery using LaGaO<sub>3</sub> based oxide ion conductor, *RSC Adv.*, 3 (2013), 8820-8825.
- [2.4] N. Xu, X. Li, X. Zhao, J. B. Goodenough, K. Huang, A novel solid oxide redox flow battery for grid energy storage, *Energy Environ. Sci.* 4 (2011) 4942-4946.
- [2.5] X. Zhao, Y. Gong, X. Li, N. Xu, K. Huang, Performance of Solid Oxide Iron-Air Battery Operated at 550°C, *J. Electrochem. Soc.*, 160 (2013), A1241-A1247.
- [2.6] M. Guo, X. Zhao, R. E. White, K. Huang, A Multi-Physics Model for Solid Oxide Iron-Air Redox Flow Battery: Simulation of Discharge Behavior at High Current Density, *J. Electrochem. Soc.*, 160 (2013), A2085-A2092.
- [2.7] A. Inoishi, S. Ida, S. Uratani, T. Okano, T. Ishihara, High capacity of an Fe-air rechargeable battery using LaGaO<sub>3</sub>-based oxide ion conductor as an electrolyte, *Phys. Chem. Chem. Phys.*, 14 (2012), 12818-12822.
- [2.8] H. Landes, R. Reichenbacher, Enhancement of Oxygen Transport in the Storage Electrode of a High Temperature Secondary Metal-Air Battery Based on an Oxygen Ion Conducting Electrolyte, *ECS. Trans.*, 50(25) (2013), 47-68.

- [2.9] W. Drenckhahn, H. Greiner, M. Kuhne, H. Landes, A. Leonide, K. Litzinger, C. Lu, C. Schuh, J. Shull, T. Soller, A Novel High Temperature Metal - Air Battery, *ECS.Trans.*, 50(45) (2013), 125-135.
- [2.10] N. H. Menzler, A. Hospach, L. Niewolak, M. Bram, O. Tokariev, C. Berger, P. Orzessek, W. J. Quadackers, Q. Fang, H. P. Buchkremer, Power-To-Storage - The Use of an Anode-Supported Solid Oxide Fuel Cell as a High-Temperature Battery, *ECS.Trans.*, 57 (2013), 255-267.
- [2.11] H. Ohmori, S. Uratani, H. Iwai, Numerical simulation of gas diffusion effects on charge/discharge characteristics of a solid oxide redox flow battery, *J. Power Sources*, 208 (2012), 383-390.
- [2.12] H. Iwai, H. Ohmori, K. Itakura, M. Saito, H. Yoshida, Numerical Prediction of System Efficiency of Solid Oxide Redox Flow Battery During Charge/Discharge Process, *ECS Trans.*, 57 (2013), 2661-2670.



## **Chapter 3**

# **System round-trip efficiency of SOIAB**

### **3.1. Numerical modeling**

#### **3.1.1. Conditions and assumptions**

For system round-trip efficiency analysis, two-container configuration shown in Fig. 2.2 is adopted. Although the operation of a rechargeable battery is unsteady, we assume that the system is in a quasi-steady state in both the charge and discharge modes. This is because our 1-D and 2-D unsteady simulations [3.1-2] explained in Chapters 4 and 5 showed that a marked decline in performance occurred only in the last 5% of each charge/discharge process when the reactants were almost consumed. It is also expected that, in a practical application, the operation mode of the system will be changed before it experiences a marked decline in performance.

The charging time,  $t_C$ , and discharging time,  $t_D$ , are assumed to be 10 and 5 h, respectively, corresponding to a daily charge/discharge cycle. Concerning the average current densities,  $i_C$  and  $i_D$ , during the charge/discharge processes, respectively, from the relationship  $t_C i_C = t_D i_D$ , we fix  $i_C$  at 50 mA/cm<sup>2</sup> and  $i_D$  at 100 mA/cm<sup>2</sup>. The output electricity in the discharge process is fixed at 5 kWh for all calculations in this study. Because the duration of the discharge process is 5 h, the system is a 1-kW-class system in the fuel cell mode. Considering that the terminal voltage of a single cell is approximately 1 V, the required total electrode area is approximately 1 m<sup>2</sup> for  $i_D$  of 100 mA/cm<sup>2</sup>.

Here, to provide a clearer view of a system, an example of a possible cell/stack geometry is presented, although it is not necessary to specify the cell geometries in this study based on 0-D models of the components. Because the compactness of the system is an important factor for a home-use application, we assume microtubular cells of 2 mm diameter [3.3-4]. Taking the example reported in ref. [3.3] of a 1 cm × 4.6 cm × 3 cm (=  $W \times H \times L$ ) module consisting of 45 cells (3 cells in width direction × 15 cells in height direction), 20 modules are necessary to provide the required electrode surface area. Hence, we assumed a stack core of 10 cm × 9.2 cm × 17.7 cm having 900 cells (30 cells in both width and height directions).

The operating temperatures of the SOEC and the Fe box are assumed to be the same for simplicity and are kept constant at 600 °C. Both the SOEC and the Fe box are thermally insulated from their surroundings. The area-specific resistances of the SOEC associated with ohmic loss and activation overpotential are estimated from experiments on microtubular cells performed at 600 °C [3.4], and they are set at  $ASR_{ohm}=0.10 \Omega\text{cm}^2$

and  $ASR_{act}=0.25 \text{ } \Omega\text{cm}^2$ , respectively. Although the activation overpotential in the electrolysis mode is generally different from that in the fuel cell mode, the same area-specific resistances are assumed in this study for simplicity. The concentration overpotential is assumed to be small and is neglected.

We also assume that the redox reaction reaches its equilibrium state at the exit of the Fe box. The composition of the hydrogen/steam mixture gas is determined accordingly, and the gas is supplied to the SOEC. When the Fe box operates at 600 °C, the hydrogen molar fraction at the SOEC inlet is 0.75. To avoid a low concentration of the reactant near the exit of the SOEC, we set a relatively low fuel utilization factor compared with that of a standard SOFC. The fuel utilization factor is set at 0.5. Note that a low fuel utilization factor does not imply that energy is wasted because the fuel gas is fully circulated. The air utilization factor of SOFCs varies with the system but is generally within the range of 0.15-0.45. It is set at 0.3 in this study.

Dry air ( $\text{N}_2 : \text{O}_2 = 0.79 : 0.21$ ) is supplied to the air blower at 25 °C. The pressure at the blower inlet is atmospheric pressure in both the air and fuel flows. The fuel-side blower must be operated at an elevated temperature. Considering the upper limit of the temperature of a blower that can be used in a small battery system for residential application, we assume that the maximum allowable blower temperature is 150 °C. Because of the low flow rates in the system, the pressure drops in both the air and fuel passages were neglected.

The calculation conditions explained above are set as the base conditions and are summarized in Table 3.1. The parameters are kept unchanged unless otherwise specified. The effects of the operation conditions are discussed in sections 3.2.3-3.2.5.

Table 3.1 Base operating conditions

Fe box	600 °C
SOEC	600 °C
Air blower	25 °C
Charge current density	50 mA/cm <sup>2</sup>
Discharge current density	100 mA/cm <sup>2</sup>
Fuel utilization	0.5
Air utilization	0.3

### 3.1.2. System round-trip efficiency

For a rechargeable battery, the ratio of the output electricity,  $P_D$ , to the input electricity,  $P_C$ , is of primary interest. It basically represents the round-trip efficiency of an SOEC as a reversible cell that functions in both fuel cell and electrolysis modes. To discuss the round-trip efficiency of the SOIAB system, we also need to consider the thermal energy input to the system because the system requires a sufficient amount of heat. We define the system round-trip efficiency,  $\eta$ , as

$$\eta = \frac{P_D}{P_C + Q_C + Q_D} \quad (3.1)$$

where  $Q_C$  and  $Q_D$  are the heat inputs to the system during the charge and discharge processes, respectively. In the calculation of the system round-trip efficiency, they are allowed to take non-negative values. If there is excess heat generation in the system

during any process, we assume that the excess heat is exhausted to the atmosphere and  $Q_C$  or  $Q_D$  is set to zero when calculating the system round-trip efficiency.

Note that, as shown below, there is a simple relationship between  $P_C$  and  $P_D$  under the assumptions employed in this study. First, the electromotive force,  $E$ , of the SOEC is obtained from the Nernst equation as

$$E = -\frac{\Delta G^0}{2F} + \frac{RT}{2F} \ln \left( \frac{p_{\text{H}_2} p_{\text{O}_2}^{1/2}}{p_{\text{H}_2\text{O}}} \right), \quad (3.2)$$

where  $\Delta G^0$ ,  $F$ ,  $R$ ,  $T$  and  $p_j$  are the change in the standard Gibbs free energy, the Faraday constant, the gas constant, the temperature and the average partial pressure of species  $j$ , respectively. Next, considering the ohmic loss and activation overpotential, the terminal voltage of the SOEC in the charge/discharge process can be expressed as

$$V_C = E + \eta_C = E + i_C \times (ASR_{ohm} + ASR_{act}), \quad (3.3)$$

$$V_D = E - \eta_D = E - i_D \times (ASR_{ohm} + ASR_{act}) \quad (3.4)$$

where  $V_C$ ,  $V_D$ ,  $\eta_C$  and  $\eta_D$  are the terminal voltages and potential losses in the charge/discharge process, respectively. Consequently, the input electrical energy in the charge process,  $P_C$ , can be calculated as

$$P_C = P_D \times \frac{V_C}{V_D} \quad (3.5)$$

### 3.1.3. Generation/absorption of thermal energy and heat transfer

#### 3.1.3.1. Reaction heat

##### During charge process

In the SOEC, heat is absorbed via the reaction expressed by Eq. 2.5. Since the reaction heat at the SOEC during the charge process,  $Q_{C,SOEC}$ , is related to the product of the temperature,  $T$ , and the entropy change,  $\Delta S$ , it can be expressed as

$$Q_{C,SOEC} = n_{H_2} \times (-T_{SOEC} \Delta S_{Eq.2.5}), \quad (3.6)$$

where  $n_{H_2}$  is the total amount of  $H_2$  that reacts in a charge operation. Heat is also absorbed by the Fe box via the reaction expressed by Eq. 2.6. The reaction heat in the Fe box during the charge operation,  $Q_{C,Fe-box}$ , is related to the enthalpy change (reaction heat),  $\Delta_r H$ , and can be expressed as

$$Q_{C,Fe-box} = n_{H_2} \times \Delta_r H_{Eq.2.6}. \quad (3.7)$$

##### During discharge process

Similarly, heat is generated by the reactions expressed by Eqs. 2.2 and 2.3. The reaction heat at the SOEC during the discharge operation,  $Q_{D,SOEC}$ , is related to Eq. 2.2 and is expressed as

$$Q_{D,SOEC} = n_{H_2} \times (-T_{SOEC} \Delta S_{Eq.2.2}). \quad (3.8)$$

The reaction heat in the Fe box during the discharge operation,  $Q_{D,Fe-box}$ , is related to Eq. 2.3 and can be expressed as

$$Q_{D,Fe-box} = n_{H_2} \times \Delta_r H_{Eq.2.3} = -Q_{C,Fe-box}. \quad (3.9)$$

Note that  $Q_{D,SOEC}$  and  $Q_{D,Fe-box}$  are both negative since these reactions are *exothermic*.

### 3.1.3.2. Losses in SOEC

There is also heat generation associated with the ohmic loss and activation overpotential in the SOEC during both charge and discharge operations. The amount of heat generated during the charge/discharge operation are expressed as  $Q_{C,\eta}$  and  $Q_{D,\eta}$ , respectively. The heat is expressed in the following forms;

$$Q_{C,\eta} = \frac{P_C}{V_C} \times \eta_C, \quad Q_{D,\eta} = \frac{P_D}{V_D} \times \eta_D. \quad (3.10)$$

In the calculation of system round-trip efficiency, the losses in the SOEC are regarded as losses in electrical energy. Therefore, the generated heat expressed by Eq. 3.10 is not counted as a heat input to the system, although it is clearly a heat-generating phenomenon occurring in the system.

### 3.1.3.3. Gas preheating

To maintain a high operation temperature, the gas flows must be preheated. The maximum allowable fuel-blower temperature is 150 °C as mentioned earlier. The mixture gas of hydrogen and steam must be cooled after it passes through the Fe box and heated again before it enters the SOEC. In a simple system without thermal recirculation, the amounts of heat required to preheat the air and fuel,  $Q_{air}$  and  $Q_{fuel}$ , are expressed as

$$Q_{air} = (c\dot{m})_{air} \times (T_{SOEC} - T_{ambient\_air}) \times t, \quad (3.11)$$

$$Q_{fuel} = (c\dot{m})_{fuel} \times (T_{SOEC} - T_{fuel\_blower}) \times t, \quad (3.12)$$

where  $c$ ,  $\dot{m}$  and  $t$  are the heat capacity of the mixture gas, the mass flow rate and the time, respectively, while  $T$  is the temperature at each location. The heat capacities

$(\dot{m})_{air}$  and  $(\dot{m})_{fuel}$  are evaluated from the gas composition and flow rate in each charge/discharge operation. Gas properties are evaluated at the mean temperature.

### 3.1.3.4. Heat inputs to system during charge and discharge processes

The total heat input during the charge and discharge operation,  $Q_C$  and  $Q_D$ , respectively, are obtained by summing all the terms related to the heat input/output except for the heat generated by the losses in the SOEC. Thus,  $Q_C$  and  $Q_D$  are expressed as

$$Q_C = Q_{C,Fe-box} + Q_{C,SOEC} + Q_{C,air} + Q_{C,fuel}, \quad (3.13)$$

$$Q_D = Q_{D,Fe-box} + Q_{D,SOEC} + Q_{D,air} + Q_{D,fuel}. \quad (3.14)$$

Note that the heat is outgoing if the sign of the variables is negative as shown in Fig. 3.1 (a).

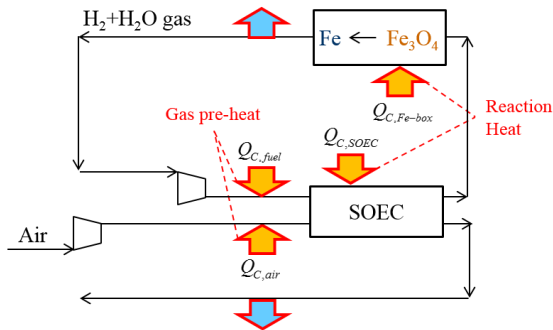
The reduction of  $Q_{air}$  and  $Q_{fuel}$  is effective for enhancing the system round-trip efficiency. In the discharge operation, it is possible to cancel the heat input with the heat output caused by the *exothermic* reactions at the SOEC and the Fe box. In the charge operation, however, the heat input is dominant.

### 3.1.3.5. Heat inputs to system with thermal recirculation

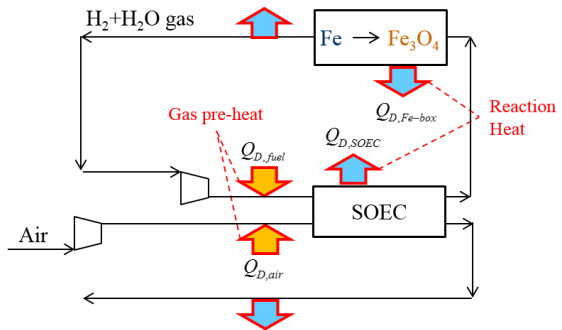
To reduce  $Q_{air}$  and  $Q_{fuel}$ , we also discuss the case with thermal recirculation using three heat exchangers (HEX1, HEX2 and HEX3) as shown in Fig. 3.1 (b). HEX1 carries heat from the hot fuel at the Fe box outlet to the cool fuel at the fuel blower outlet, HEX2 carries heat from the hot fuel at the fuel blower inlet to the cool air at the air blower outlet, and HEX3 carries heat from the hot air at the SOEC outlet to the cool air at the

(a) The system in which the thermal energy required to preheat the gases is considered.

(Charge)



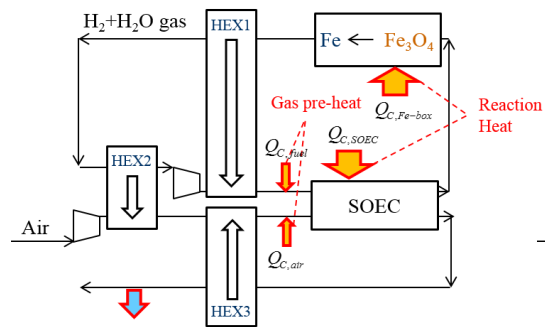
(Discharge)



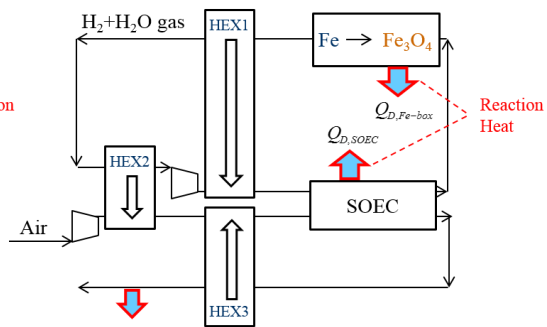
Orange arrow: Major heat input to the system, Blue arrow: Major heat output from the system

(b) The system with three heat exchangers.

(Charge)



(Discharge)



Orange arrow: Major heat input to the system, Blue arrow: Major heat output from the system, White arrow: Heat flow direction inside the heat exchangers

Figure 3.1. Main heat input/output of the system (a) The system in which the thermal energy required to preheat the gases is considered, (b) The system with three heat exchangers.

SOEC inlet. They help to preheat the gases and reduce  $Q_{air}$  and  $Q_{fuel}$ . For all the heat exchangers, the heat exchanger effectiveness was fixed at 0.85 during the charge process).

## 3.2. Results and discussion

### 3.2.1. Energy budget of fundamental system without thermal recirculation

To clarify fundamental characteristics of the SOIAB, we start with a preliminary discussion of a simple system and stepwisely take more realistic factors into account. In the first step (Case 1), we focus only on the SOIAB and neglect the thermal energy required to preheat the gases. Also, we assume an ideal SOEC with no IR loss or overpotential. Under these two assumptions,  $Q_C$  and  $Q_D$  include only the reaction heats expressed by Eqs. 3.6-3.9, and the Sankey diagram of the Case 1 can be simplified as shown in Fig. 3.2. A Sankey diagram shows the energy flow in a system. The white rectangle shown in the center corresponds to the chemical energy stored as reduced iron. The left side and right side correspond to the charging and discharging process, respectively. The upper arrow (green) shows the electric energy while the lower arrow (red) shows the thermal energy. The system round-trip efficiency in the electrical energy budget is 100% ( $P_D/P_C = 1.0$ ). If we consider the thermal input for endothermic reactions of Eqs. 2 4-2.6, however, the round-trip efficiency of this ideal system is evaluated to be 73% from Eq. 3.1.

In the second step (Case 2), when the effects of the IR loss and activation overpotential in the SOEC are considered, the input electrical energy should be increased to maintain the output electrical energy. The Sankey diagram of this case is shown in Fig. 3.3. The ratio of the electric output to the electric input,  $P_D/P_C$ , becomes 0.95; thus, the effects of the losses are not significant under the assumptions employed in this study.

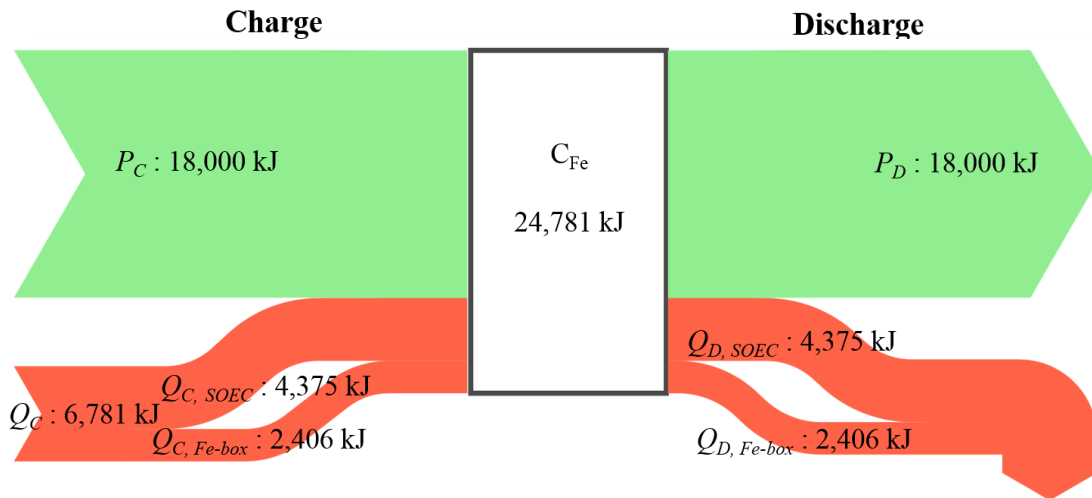


Figure 3.2. Sankey diagram of SOIAB (Case 1). It assumes there is no loss in the SOEC. Only the reaction heat associated with the electrochemical reaction and the redox reaction are considered as the heat input/output. Numbers are the amount of energy in kJ.

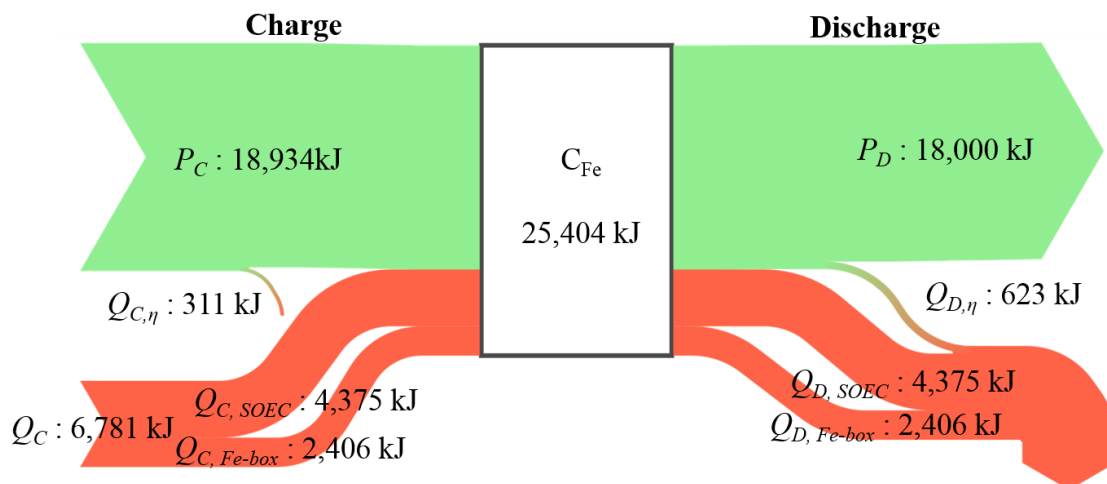


Figure 3.3. Sankey diagram of SOIAB (Case 2). The effects of IR loss and the activation overpotentials in the SOEC are added to the conditions of Case 1.

Note that Xu et al. [3.5] achieved  $P_D/P_C = 0.92$  in their lab-scale experiment. The system round-trip efficiency considering the thermal input for supplementation of the reaction heat slightly decreases owing to the internal losses in the SOEC and becomes 70%.

In the third step (Case 3), we consider the thermal energy required to preheat the supply gases,  $Q_{air}$  and  $Q_{fuel}$  expressed by Eqs. 3.11 and 3.12, respectively. For the case without thermal recirculation by the heat exchangers, the starting temperatures of the air flow and fuel flow are 25 °C and 150 °C, respectively. For this case, a Sankey diagram is shown in Fig. 3.4, which shows the energy flow in the system.  $C_{Fe}$  (white) shown in the center corresponds to the chemical energy stored as reduced iron. The left and right sides correspond to the charge and discharge operations, respectively. The upper arrow (green) shows the electrical energy while the lower arrow (red) shows the thermal energy. The figures shown next to the variables are the amounts of energy in kJ. The value of  $P_D/P_C$  remains at 0.95, the same as before. As can be clearly seen from the figure, the amount of thermal energy required to preheat the gases is relatively large, and the resulting system round-trip efficiency drops to as low as 26%. Thus, to improve the system round-trip efficiency, efficient thermal recirculation of the gas flows is considered to be indispensable as described in the next section

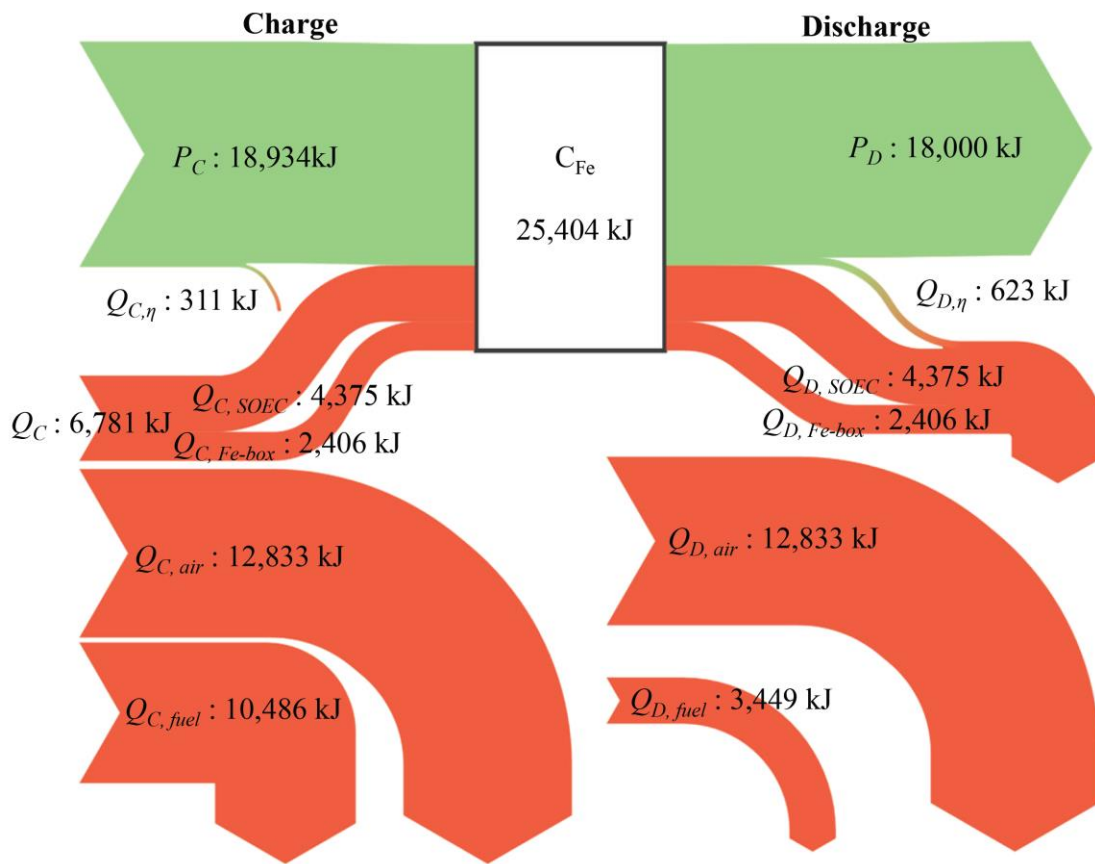


Figure 3.4. Sankey diagram of SOIAB (Case 3). The thermal energy required to preheat the gases is considered.

### **3.2.2. Energy flows in SOIAB system with thermal recirculation**

Because preheating the gas requires most of the heat input in a relatively small 5 Wh system we previously introduced the system with three heat exchangers in section 3.1.3.5 (Fig. 3.1 (b)). Table 3.2 summarizes the gas temperatures at various characteristic positions in the charge/discharge process. The energy flow for the present case is shown as a Sankey diagram in Fig. 3.5. The system round-trip efficiency increases to 61%, which shows the striking impact of thermal recirculation. The ratio of the electric output to electric input,  $P_D/P_C$ , remains the same as that in section 3.2.1 (0.95).

Since the thermal energy input to preheat the gases is markedly less than that shown in Fig. 3.4, the reaction heat in the charge process becomes the main component of the heat input. To further reduce the heat input, the use of a regenerator (a storage-type heat exchanger) that recovers the heat exhausted during the discharge process is also an attractive method. Considering the heat-loss penalty of a small-scale regenerator, however, the use of a regenerator is more suitable for large-scale systems. Furthermore, a regenerator requires the operating temperature to be higher in the discharge process than in the charge process. The implementation of a regenerator in the system will be discussed elsewhere and is beyond the scope of this study.

For operation under the base conditions discussed above, in sections 3.3 to 3.5, we examine the effects of various parameters on the round-trip efficiency of the system to investigate its characteristics in detail. Only the parameter explicitly stated is varied while the other calculation conditions are fixed at the base conditions.

Table 3.2 Gas temperatures at various points in the system under the base operating conditions

Charge:

	Path	Gas	In	Out
HEX1	Hot side	Fuel	600 °C	136 °C
	Cold side	Fuel	49 °C	517 °C
HEX2	Hot side	Fuel	136 °C	49 °C
	Cold side	Air	25 °C	119 °C
HEX3	Hot side	Air	600 °C	223 °C
	Cold side	Air	119 °C	528 °C
Fuel Blower		Fuel	49 °C	-

Discharge:

	Path	Gas	In	Out
HEX1	Hot side	Fuel	600 °C	89 °C
	Cold side	Fuel	26 °C	540 °C
HEX2	Hot side	Fuel	89 °C	26 °C
	Cold side	Air	25 °C	48 °C
HEX3	Hot side	Air	600 °C	202 °C
	Cold side	Air	48 °C	432 °C
Fuel Blower		Fuel	26 °C	-

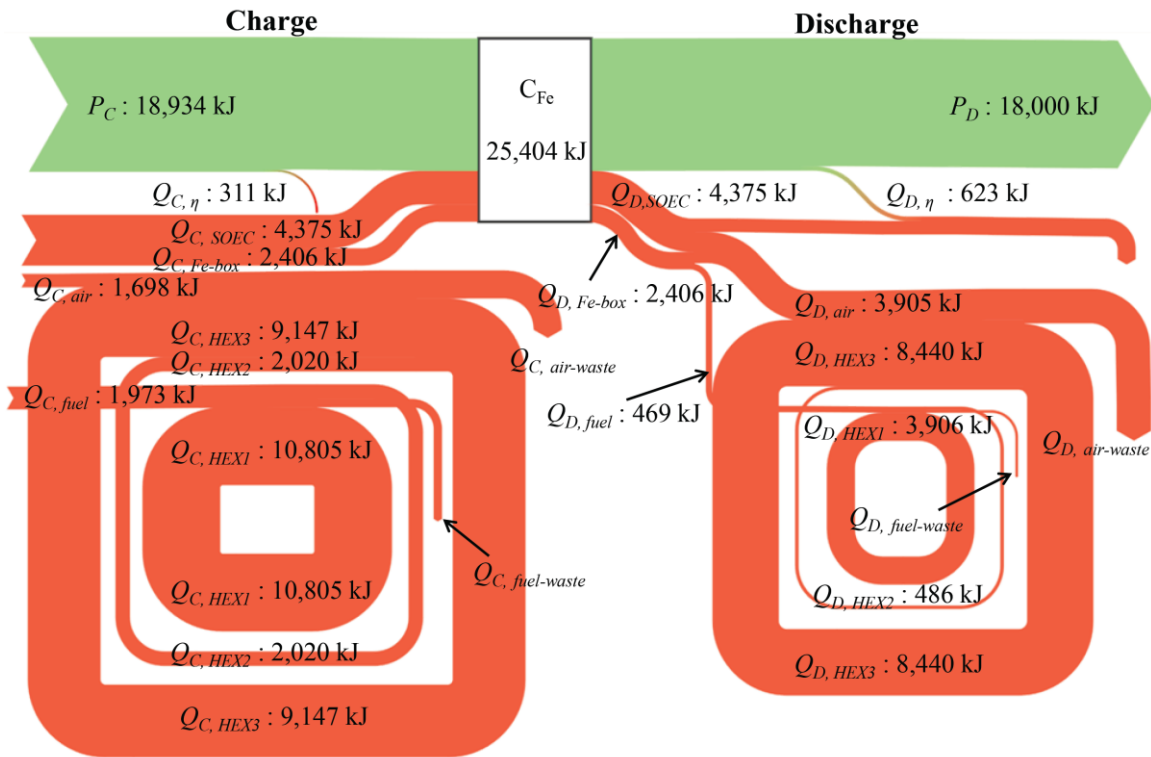


Figure 3.5. Sankey diagram of SOIAB system with three heat exchangers (Case 4).

### 3.2.3. Effects of heat exchanger effectiveness on round-trip efficiency

Figure 3.6 shows the effects of the heat exchanger effectiveness on the system round-trip efficiency. Here, the effectiveness of one heat exchanger is varied while maintaining the values for the other two heat exchangers at 0.85. The figure shows that the effectiveness of HEX3 has a strong effect on the system round-trip efficiency. This is reasonable because the amount of heat exchanged by HEX3 is the largest among the three heat exchangers. Higher system round-trip efficiency is expected when the effectiveness of HEX3 is high. At the point marked with a square, which is “a heat-balanced point”, the input heat during the discharge process,  $Q_D$ , is equal to zero. When the effectiveness of HEX3 decreases and passes over the heat-balanced point, the slope of the round-trip efficiency becomes steeper since  $Q_D > 0$ . This means that heat must be input to the system even in the discharge operation, which reduces its round-trip efficiency. The effectiveness of HEX1 also substantially affects the round-trip efficiency. When the effectiveness of HEX1 is reduced, the heat input required to preheat the fuel gas increases. This leads to a decrease in the round-trip efficiency. On the other hand, the effect of HEX2 on the system round-trip efficiency is not significant. The line comes to an end at a point marked “x” in this case. This mark corresponds to the state where the temperature of the fuel mixture gas at the blower reaches the maximum allowable blower temperature (150 °C).

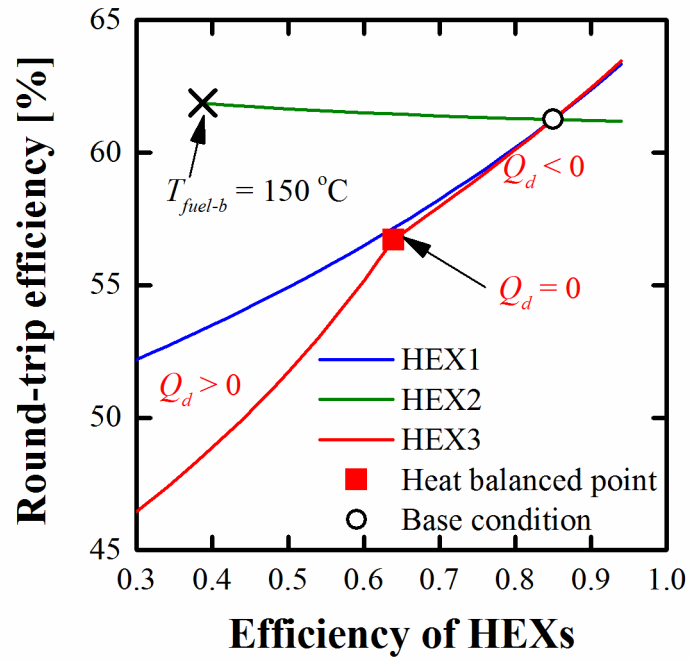


Figure 3.6. Effects of heat exchanger effectiveness on the system round-trip efficiency.

### 3.2.4. Effects of gas utilization factors on round-trip efficiency and efficient and uniform operation

The effects of the gas utilization factors are shown in Fig. 3.7. The fuel and air utilization factors are set at 0.5 and 0.3 under the base conditions, respectively. The system round-trip efficiency increases with increasing air or fuel utilization factor. This is because the fuel/air flow rate decreases at a higher utilization factor, which reduces the energy required for the preheating of the gas. Because the air flow rate is generally higher than the fuel flow rate, the effect of the air utilization factor on the round-trip efficiency is more prominent. In particular, in the region where the air utilization factor is below the heat-balanced point,  $Q_D > 0$ , the slopes become very steep and the system round-trip efficiency markedly drops. This shows the importance of operating the system under conditions where no heat input is required in the discharge operation. The maximum allowable blower temperature gives the lower limit for the fuel utilization factor and the higher limit for the air utilization factor.

In Fig. 3.7 (a), the calculation covers a very high fuel utilization condition. Note that the effect of fuel depletion will appear in an actual system when the fuel utilization factor is very high. Because the hydrogen molar fraction at the SOEC inlet is approximately 0.75 (the equilibrium value at 600 °C), its value at the SOEC exit becomes less than 0.15 when the fuel utilization factor is over 0.8 in the discharge operation. To observe the effects of the gas utilization factors within the limitation of the 0-D model simulation, we calculate the EMF at the SOEC exit,  $E_{out}$ , for each combination of fuel and air utilization factors, which is normalized by the EMF at the inlet,  $E_{in}$ , and is shown in Fig. 3.7 (b) as black contour lines. A lower value of  $E_{out}/E_{in}$

means a large variation of the local EMF within a single cell, which also indicates an associated non-uniformity of the local current density, temperature and overpotential distributions. In Fig. 3.7 (b), the combination of the fuel and air utilization factors that gives the heat-balanced condition is depicted with a blue line. To avoid the condition of  $Q_D > 0$ , for which a low round-trip efficiency is expected, the system must be operated in the region to the right of the curved blue line in the figure. On the other hand, the red line in Fig. 3.7 (b) indicates the limit at which the fuel-blower

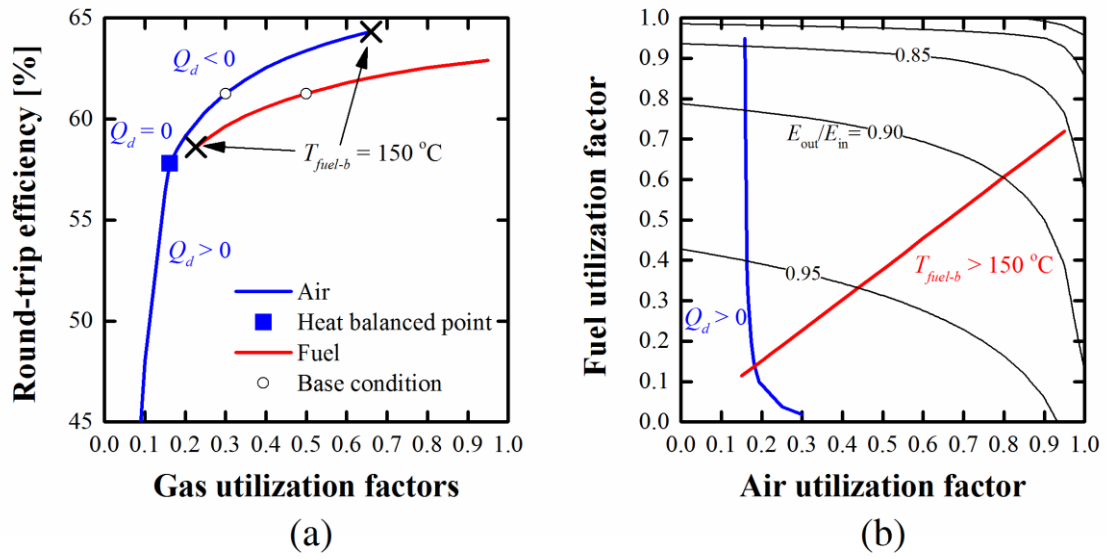


Figure 3.7. Effects of the fuel and air utilization factors on the system (a) Round-trip efficiency, (b) Operating window for the efficient and uniform operation of the system.

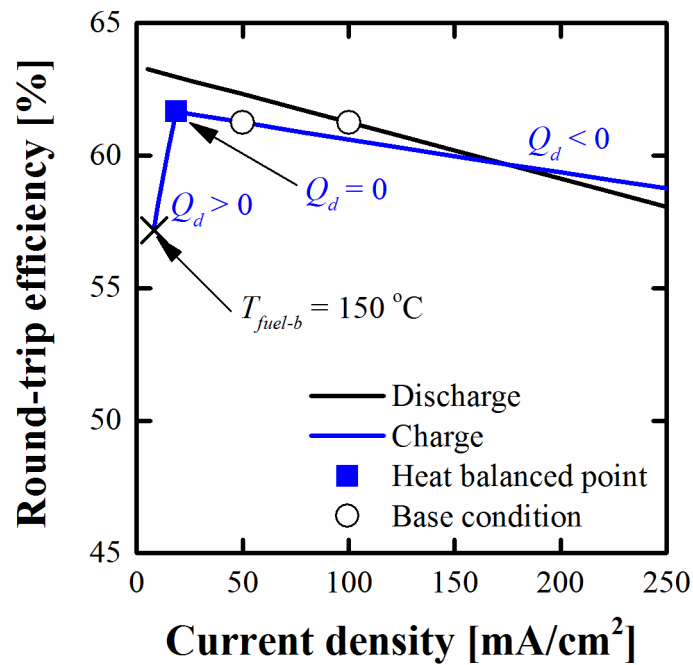


Figure 3.8. Effects of the current density on the system round-trip efficiency.

temperature reaches its maximum allowable value of 150 °C; the system must be operated in the region to the left of the red line in the figure. Consequently, the acute-angled region bounded by the blue and red lines in Fig. 3.7 (b) shows conditions for efficient and uniform operation under the constraints set in this study. For example, if we assume an allowable lower limit of  $E_{out}/E_{in}$  is 0.9, the system should be operated within the triangular region formed by the blue line, red line and black line for  $E_{out}/E_{in} = 0.9$ . As a result, the set of conditions for an efficient and uniform operation is obtained.

### **3.2.5. Effects of current density on round-trip efficiency**

As shown in Fig. 3.8, the round-trip efficiency changes with the current density during the charge or discharge operation. Again, note that the operation time changes with the current density according to the relationship  $t_C i_C = t_D i_D$ . As the current density of either operation is increased, the round-trip efficiency decreases because the electrical energy loss during the operation increases owing to higher internal losses. The marked change in the round-trip efficiency observed under the low-current-density condition in the charge operation is caused by the insufficient performance of the heat exchangers during the discharge operation. As explained in section 3.1.3.5, the heat exchangers are designed to meet the requirement for the charge operation in this study. If the current density in the charge operation is low, the required heat transfer surface area of the HEXs decreases owing to the low flow rates. The area, however, is insufficient for the discharge operation. This results in an insufficient heat recovery for

the preheating of air during the discharge operation. The demand for additional heat input during the discharge operation increases, lowering the round-trip efficiency.

### 3.3. Summary

A system simulation model of an SOIAB system was developed to investigate the fundamental characteristics during the charge and discharge operations. The simulation was conducted under a quasi-state assumption with 0-D models of the system components, i.e., the SOEC, the Fe box and the heat exchangers. To clarify the energy balance and also improve the system round-trip efficiency, special care was taken when considering thermal aspects; not only a simple system but also a more complicated system with thermal recirculation by three heat exchangers was investigated. That is, we first defined the system round-trip efficiency in which the thermal energy as well as the electrical energy is properly taken into account. Regarding thermal recirculation, we discuss the effects of the factors practically imposed on heat exchangers, such as the temperature limit and heat exchanger effectiveness. The specific conclusions obtained in this study are summarized as follows:

(1) The theoretical round-trip efficiency of an ideal system is 73% at 600 °C. Approximately 30% of the input energy is lost as reaction heat during the discharge operation. The heat generation associated with the overpotentials in the SOEC is insignificant compared with the reaction heat. When the thermal input to preheat the gases is considered, the system round-trip efficiency decreases to as low as 26%. This is because the heat required to preheat the gases is much larger than the reaction heat. The system round-trip efficiency can be recovered by introducing heat exchangers to circulate thermal energy from the exhaust gases. By utilizing heat exchangers, the system round-trip efficiency recovers to 61% under the base conditions. Therefore, it is

considered that the SOIAB has a potential to be utilized as a practical energy storage device.

(2) The effects of the heat exchanger effectiveness, gas utilization and current density were examined. The effectiveness of HEX1 or HEX3 has a noticeable impact on the system round-trip efficiency, while that of HEX2 has little effect. A higher fuel/air utilization factor is generally preferred from the view point of round-trip efficiency. There is, however, an upper limit for the air utilization factor because the maximum allowable fuel-blower temperature becomes a constraint. It also gives a lower limit for fuel utilization. The operation conditions under which heat input is required even during the discharge operation were clarified for each parameter examined. The system round-trip efficiency considerably drops under these operation conditions. This constraint gives a lower limit for the air utilization factor. By considering the effects of the gas utilization factors, a window for operation was obtained in the air utilization and fuel utilization plane. The thermal management at the elevated temperature for decreasing the heat loss is a key to improve of the system round-trip efficiency.

## References

- [3.1] H. Ohmori, S. Uratani, H. Iwai, Numerical simulation of gas diffusion effects on charge/discharge characteristics of a solid oxide redox flow battery, *J. Power Sources* 208 (2012) 383-390.
- [3.2] H. Ohmori, H. Iwai, Simulation of solid oxide iron-air battery: Effects of heat and mass transfer on charge/discharge characteristics, *J. Power Sources* 286 (2015) 264-275.
- [3.3] Y. Funahashi, T. Suzuki, Y. Fujishiro, T. Shimamori, M. Awano, 200 W module design using micro tubular SOFCs stacks and systems, *ECS Trans.* 25 (2009) 195-200.
- [3.4] T. Suzuki, Z. Hasan, Y. Funahashi, T. Yamaguchi, Y. Fujishiro, M. Awano, Impact of anode microstructure on solid oxide fuel cells, *Science* 325 (2009) 852-855.
- [3.5] N. Xu, X. Li, X. Zhao, J. B. Goodenough, K. Huang, A novel solid oxide redox flow battery for grid energy storage, *Energy Environ. Sci.* 4 (2011) 4942-4946.



# Chapter 4

## 1-D numerical simulation of mass transfer effects on SOIAB

### 4.1. Numerical procedure

#### 4.1.1. Battery design and computational domain

We assume one of the simplest battery configurations with a single package of Figs. 2.1 and 4.1. It consists of the planar SOEC, the redox metal and a container. The air-side electrode of the SOEC is exposed to the air ( $N_2 : O_2 = 0.79 : 0.21$ ) while the hydrogen-side electrode is to the hydrogen/steam mixture gas in the container. The total pressure inside the container is assumed to be constantly 1 atm. The redox metal is placed inside the container. Note that, unlike the flow-type configuration in Xu et al. [4.1], there is no bulk fluid motion in the container in this study. Focusing on the center part of the system marked as a computational domain in Fig. 4.1, we assume one-dimensional phenomena in the  $x$ -direction neglecting the sidewall effects. The main design parameters of the system are the length of the redox metal,  $L_1$ , and the distance between the SOEC and the redox metal,  $L_2$ .  $L_2$  is kept constant at 1 cm throughout this

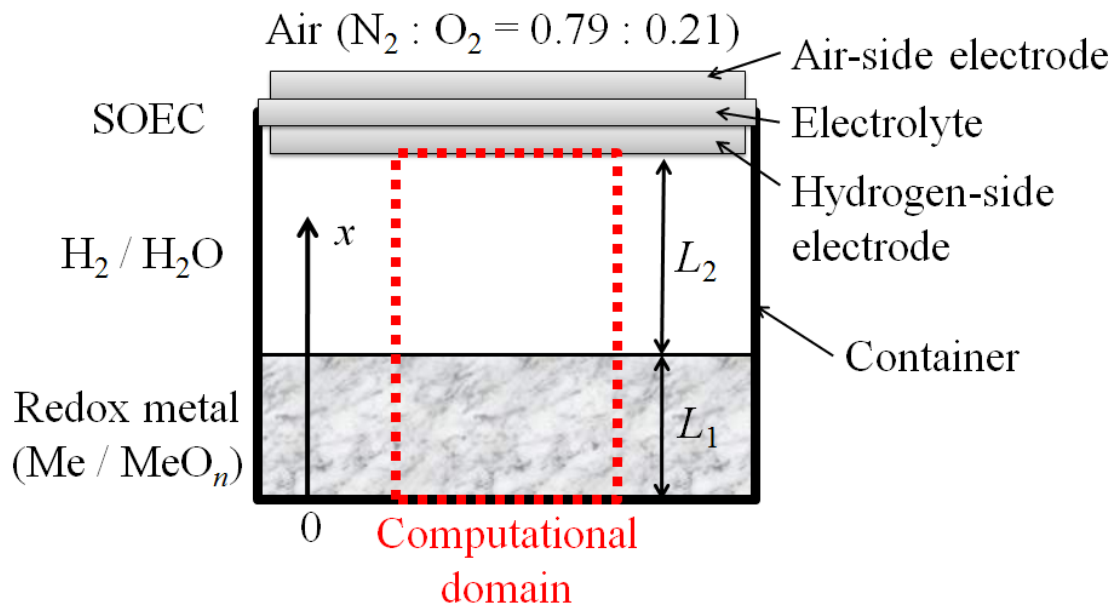


Figure 4.1. A schematic figure of the battery including the SOEC and the redox metal.

study.  $L_l$  is related to the amount of the redox metal per unit area of the SOEC electrode. As a standard condition, we place 1 g/cm<sup>2</sup> of reduced the redox metal with a porosity of 0.7 which results in  $L_l$  of 4.2 mm. We assume  $L_l$  is constant during the operation unless the amount of the redox metal is varied. As the redox metal is iron, its volume increases by a factor of 2.1 when it is oxidized. The volume expansion/reduction caused by redox reaction affects the local porosity of the redox metal.

## 4.1.2. Numerical modeling

In this paper, the distributions of the participating gas species in the system and their effects on the battery performance are major interests. 1-dimensional numerical simulation based on a mass diffusion equation is conducted to examine the dynamic behavior of the battery affected by interaction of two parallel reactions.

### 4.1.2.1. Governing equation

The governing equation is the time-dependent 1-D diffusion equation.

$$\frac{\partial Y_j}{\partial t} = \frac{\partial}{\partial x} \left( D \frac{\partial Y_j}{\partial x} \right) + S_j \quad (4.1)$$

$Y$ ,  $D$ ,  $S$  and  $j$  denote the concentration of hydrogen or steam, gas diffusion coefficient, mass production/consumption and species, respectively. Mass production/consumption is associated with the metal redox reaction. As explained in the latter sections, we assume the concentration overpotential in the SOEC electrodes is negligible. The mass production/consumption is expressed as boundary conditions on the SOEC side. On the

other hand for the redox metal, we consider the diffusion inside the porous material thus the mass production/consumption effect appears in the equation as a source term.

Inside the porous material, gas diffusion is limited and its effect is taken into account by considering an effective diffusion coefficient,  $D_{eff}$ . A precise evaluation of  $D_{eff}$  is a challenging problem itself as it depends on the microstructure of the porous material. As this study is a first step to understand the fundamental characteristics of the new battery, we treat it in a simple way as

$$D_{eff} = D \frac{\varepsilon}{\tau} \quad (4.2)$$

where  $\varepsilon$  and  $\tau$  are the porosity and tortuosity factor of the porous material. Following Melkote and Jensen [4.2], the tortuosity factor is assumed to be reciprocal of the porosity,  $\tau = 1/\varepsilon$ . We further assume that the representative pore diameter is much longer than the mean free path of hydrogen and neglect Knudsen diffusion (rarefaction effect).

#### **4.1.2.2. Metal redox reaction model**

We assume local thermal equilibrium and a large effective thermal conductivity of the porous material resulting in a uniform temperature assumption for the porous part. In a real system, its temperature is to be determined as a result of the balance of the heat generation/absorption in the system and heat loss to surroundings. For simplicity, in this study, we set a constant temperature of 400°C.

We performed preliminary in-house experiment using iron particles at 400°C and obtained volume specific reaction rate. It is expressed in terms of the partial pressures of

hydrogen and steam,  $p_{H_2}$  and  $p_{H_2O}$ . When hydrogen partial pressure is below the equilibrium pressure, the hydrogen generation rate is calculated as

$$S = \left\{ -\left(k_1 \times p_{H_2}\right) + \left(k_2 \times p_{H_2O}\right) \right\} \times M \quad (4.3)$$

and is applied to Eq. 4.1.  $k_1$  and  $k_2$  are reaction coefficients determined from the experiments while  $M$  is the molar density of the reactant. When hydrogen partial pressure is above the equilibrium pressure, the hydrogen consumption rate of the redox metal is calculated by the same equation with the minus.

#### 4.1.2.3. Electrochemical model of the SOEC

The SOEC was assumed to have uniform temperature of 600°C and work under uniform current density condition. Electromotive force,  $E$ , is evaluated by Nernst equation.

$$E = E^0 + \frac{RT}{2F} \ln \left( \frac{p_{H_2} \times p_{O_2}^{1/2}}{p_{H_2O}} \right) \quad (4.4)$$

$$E^0 = -\frac{\Delta G^0}{2F} \quad (4.5)$$

Here,  $E^0$ ,  $R$ ,  $T$ ,  $F$  and  $p$  are standard electromotive force, universal gas constant, temperature, Faraday constant and partial pressure, respectively. Concentration overpotential was neglected assuming thin electrodes. The area specific resistances,  $ASR$ , associated with IR loss and the activation overpotential were set as  $1e-5$  and  $2.5e-5$  [ $\Omega \cdot m^2$ ], respectively, by fitting  $i$ - $V$  curve of an experiment at 600 °C [4.3]. Although the activation overpotential in electrolysis mode is generally different from that of fuel

cell mode, the same expression was assumed in this study for simplicity. IR loss,  $\eta_{\text{ohm}}$ , and activation overpotential,  $\eta_{\text{act}}$ , are expressed as

$$\eta_{\text{ohm}} = ASR_{\text{ohm}} \times i \quad (4.6)$$

$$\eta_{\text{act}} = ASR_{\text{act}} \times i \quad (4.7)$$

where  $i$  is the current density (absolute value). Then the terminal voltage,  $V$ , can be obtained as

$$\text{Discharge :} \quad V_{\text{discharge}} = E - (\eta_{\text{ohm}} + \eta_{\text{act}}) \quad (4.8)$$

$$\text{Charge :} \quad V_{\text{charge}} = E + (\eta_{\text{ohm}} + \eta_{\text{act}}) \quad (4.9)$$

for the discharge operation and charge operation, respectively.

#### 4.1.2.4. Numerical procedure

An in-house program code was developed and was applied to the battery model shown in Fig. 4.1. The governing equations were discretized using the finite volume method. Non-uniform grid system was applied with finer grid spacing in the redox metal porous medium where a steep concentration gradient was expected. A systematic grid test was conducted to confirm that results had no grid dependency.

#### 4.1.2.5. Computational conditions

The steam/hydrogen mixture in the container is initially at equilibrium state at 600°C. The redox metal is totally reduced at the beginning of the discharge operation, while it is totally oxidized at the beginning of the charge operation. We assume the temperature of the SOEC and the mixture gas are constant at 600 °C while the redox material operates at 400 °C. The average current density of the SOEC and the amount of

the redox metal in the container are basically set at  $100 \text{ mA/cm}^2$  and  $1 \text{ g/cm}^2$ , respectively. They are varied only in sections 3-4 and 3-5 to see their effects on the operation.

## **4.2. Results and discussion**

### **4.2.1. Fundamental characteristics charge/discharge operations**

The fundamental characteristics of the battery are discussed taking the case of the current density at  $100 \text{ mA/cm}^2$ . Fig. 4.2 shows the time history of the terminal voltage under charge/discharge conditions. State of charge, SOC, is defined as the rate of electricity (Ah) stored in the battery to that of full charge. When the battery is fully charged, SOC is 100%. The terminal voltage under charge condition is naturally higher than that under discharge condition. Except for the last 10% of each operation, the redox reaction proceeds fast enough and it balances to the electrochemical reaction resulting in an almost constant terminal voltage. Under this condition, the system appears to be in a quasi-steady state. A marked rise of the terminal voltage in the charge operation at SOC larger than 90% reflects a rise of hydrogen partial pressure in the container. It is caused by limited consumption of hydrogen at the redox metal corresponding to Eq. 2.6. On the other hand, a marked decline of the terminal voltage in the discharge operation at SOC smaller than 10% reflects a decline of hydrogen partial pressure in the container. It is caused by limited generation of hydrogen at the redox metal corresponding to Eq. 2.3.

### **4.2.2. Gas diffusion during operations**

Figure 4.3 shows the distribution of hydrogen partial pressure inside the container, corresponding to Fig. 4.2. The area of  $0.0 < x < 4.2 \text{ mm}$  corresponds to the porous part with the redox metal, and the SOEC electrode surface is located at  $x = 14.2 \text{ mm}$ . Since

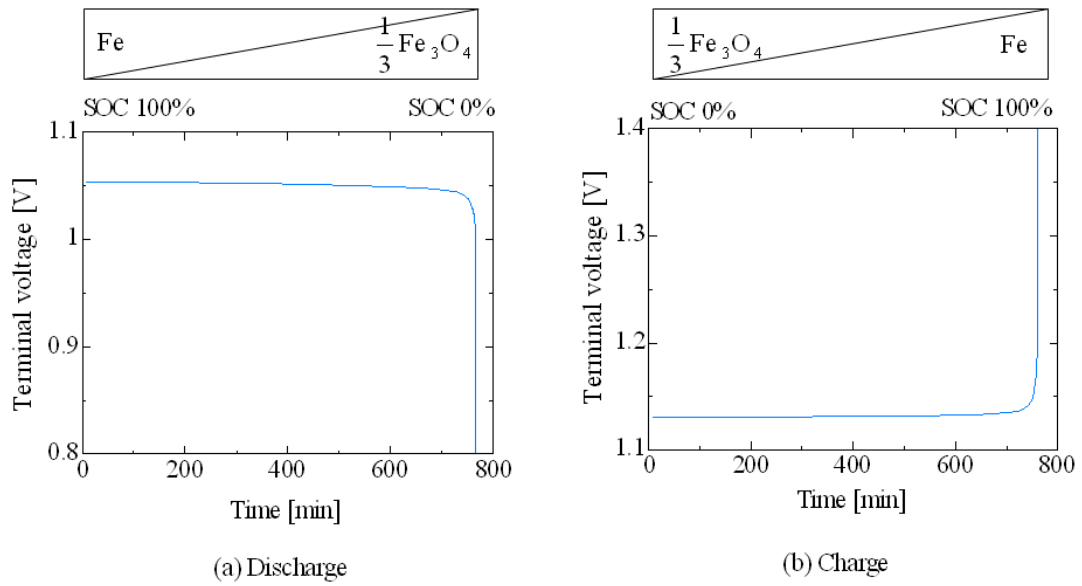


Figure 4.2. Time history of terminal voltage (a) in charge operation and (b) discharge operation at 100 mA/cm<sup>2</sup> with 1 g-Fe/cm<sup>2</sup>.

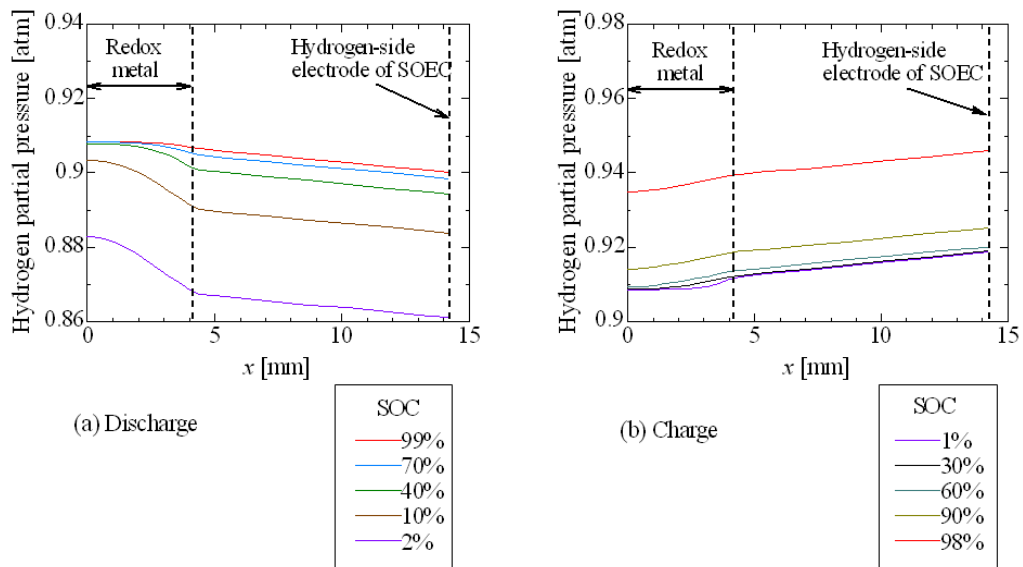


Figure 4.3. Distribution of hydrogen partial pressure in the container (a) in discharge operation and (b) in charge operation.

the mixture gas is binary, steam partial pressure can easily be calculated from Fig. 4.3. Under discharge operation, the hydrogen generated by metal oxidation diffuses to the SOEC while hydrogen diffuses in the opposite direction under charge operation. The figure shows that the partial pressure of hydrogen in the container generally takes a high value when SOC is high. Its increase/decrease during the charge/discharge process is consistent with the marked rise/decline of the terminal voltage observed in Fig. 4.2. It also shows that the distribution is relatively flat in  $x$ -direction in particular under charge operation. In both discharge/charge operations, the distribution is almost linear in the area of  $4.2 < x < 14.2$  mm. Inside the porous part, on the other hand, the gradient is not constant and generally larger reflecting the limited diffusion coefficient express by Eq. 4.2. The non-linear distribution pattern gradually changes as SOC increases/decreases. The increase of the gradient is more prominent in the discharge operation.

### **4.2.3. Evolution of redox reaction area**

Partial pressure distribution in the porous part is affected by the generation/consumption of hydrogen and steam associated with the metal redox reaction. The distribution of hydrogen-generation rate is shown in Fig. 4.4. Negative value in Fig. 4.4 (b) corresponds to the hydrogen consumption during the charge operation. As explained in the subsection 4.2.1, it is assumed that the redox metal, iron, is completely reduced at the initial state of the discharge operation and is completely oxidized at the initial state of the charge operation. Therefore the increase of SOC in charge operation and the decrease of that in discharge operation correspond to the elapsed time.

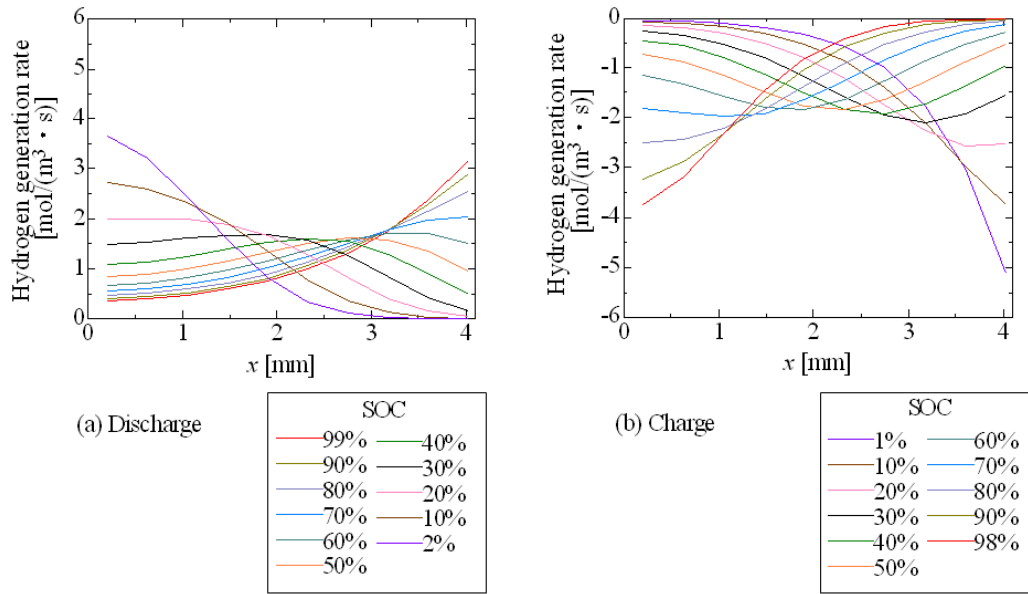


Figure 4.4. Distribution of hydrogen generation rate in the redox metal region (a) in discharge operation and (b) in charge operation.

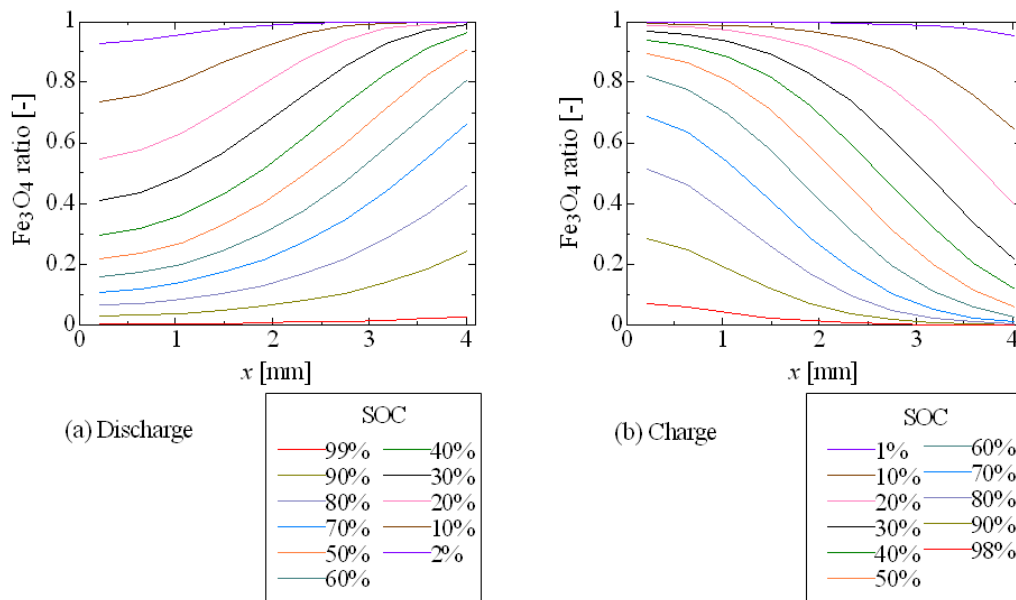


Figure 4.5. Distribution of  $\text{Fe}_3\text{O}_4$  ratio in the redox metal region (a) in discharge operation and (b) in charge operation.

During the discharge operation, steam generated at the SOEC approaches to the redox metal by diffusion. Oxidation of the metal first proceeds actively near the surface region close to the SOEC (right side in Fig. 4.4 (a)) due to relatively high steam partial pressure. As oxidation goes on, the portion of the metal oxide increases near the surface region and the active reaction region gradually shifts into the inner part where fresh reduced metal exists. The increase of the metal oxide can be confirmed in Fig. 4.5, which shows the distribution of  $\text{Fe}_3\text{O}_4$  ratio in the redox metal region. It is worth noting in Fig. 4.5 (a) that approximately 30 % of metal near  $x = 0$  is still not oxidized at SOC = 10 % in discharge operation. It is expected that the drastic decrease of the terminal voltage at SOC < 10 % observed in Fig. 4.2 (a) can be delayed by improving the gas diffusion in the redox metal. Similar shift of the active reaction region can be seen during charge operation as shown in Fig. 4.4 (b) and Fig. 4.5 (b).

Fig. 4.6 shows the distribution of local porosity in the redox metal. Because the particles expand in volume when they are oxidized, the local porosity changes depending on the degree of oxidation. At the initial state, it distributes uniformly in both discharge/charge operations. Its value is noticeably low for the charge operation because the particles are fully oxidized at the initial state. When the portion of the oxidized particle is large, local porosity is low and the effective diffusion coefficient takes a small value. The effect of the particle expansion can be clearly seen in Figs. 4.3 and 4.4. In discharge operation shown in Fig. 4.4 (a), the reaction rate at the inner region is moderate even at the beginning due to moderate diffusion through the pores. In the charge operation shown in Fig. 4.4 (b), on the other hand, the reaction rate is close to zero around the inner region at the beginning of operation because of insufficient diffusion limited by the expanded particles. In Fig. 4.3 (a), a steep partial pressure

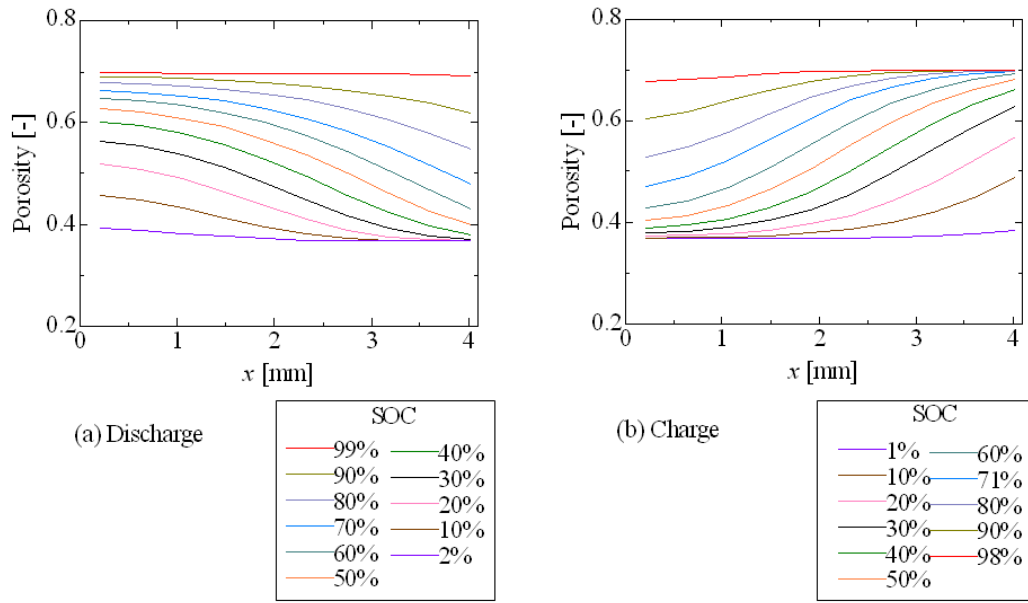


Figure 4.6. Distribution of porosity of the redox metal region (a) in discharge operation and (b) in charge operation.

gradient is formed near the surface region,  $x = 4.2$ , and it gradually expands to inner region, which agree well with the shift of the active reaction region seen in Fig. 4.4 (a). Under the calculation condition set in this study, the gas diffusion is not completely blocked by the expanded particles (metal oxide). It should be noted, however, that inappropriate filling of the particles may cause a severe decrease of the gas diffusion coefficient to cause a fatal delay of the redox reaction.

Concerning the diffusion in the space between the SOEC and the redox metal, no practical problem is observed under the calculation conditions and geometry set in this study. Diffusion inside the porous redox metal is the major mass transfer phenomenon that needs to be carefully considered.

#### **4.2.4. Effects of current density**

Figure 4.7 shows the effects of the current density on the battery operation. In discharge operation, the current density was varied in the range between 10 to 2000 mA/cm<sup>2</sup> and was kept constant during each operation. All other conditions were unchanged from the base condition discussed above. A high current density means the enhanced electrochemical reaction on the SOEC. The terminal voltage is generally low at a high current density condition, mainly because of the large ohmic and activation losses. The terminal voltage, or more precisely the EMF, is also affected by the hydrogen/steam composition at the electrode surface of the SOEC. When the current density is raised, partial pressure of steam increases. It enhances the hydrogen generation on the redox metal until the hydrogen generation and consumption balances. If two reactions balance, a quasi-steady state is established and the power generation

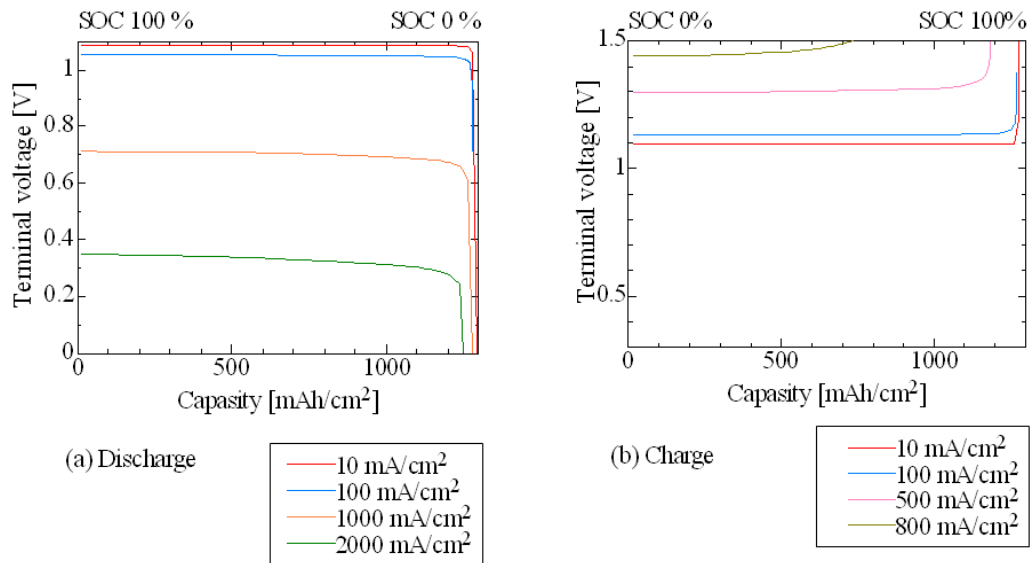


Figure 4.7. Effects of the current density on the terminal voltage with 1 g-Fe/cm<sup>2</sup> (a) in discharge operation and (b) in charge operation.

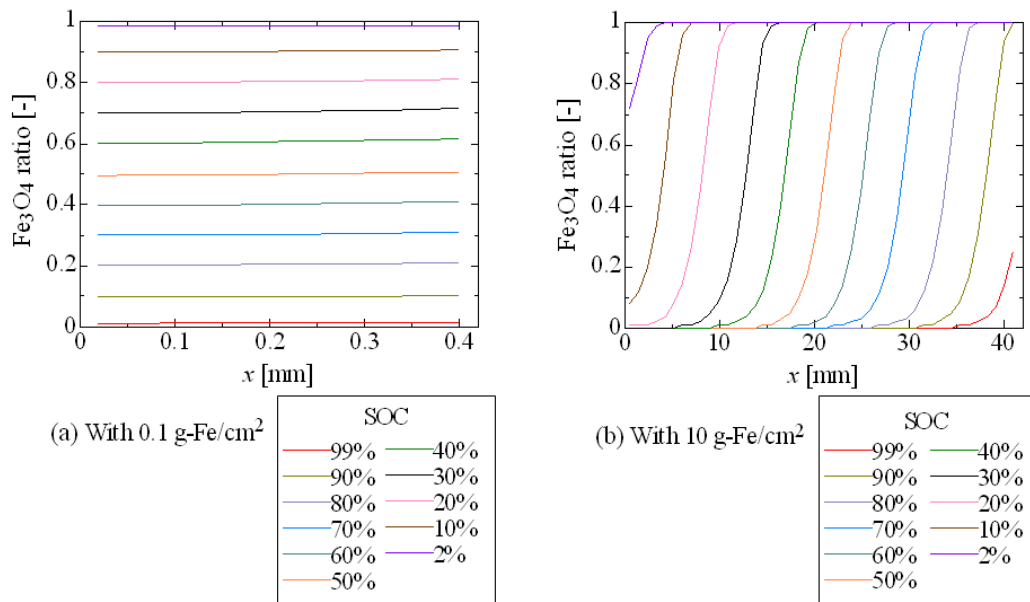


Figure 4.8. Effects of the amount of the redox metal on distribution of Fe<sub>3</sub>O<sub>4</sub> ratio in discharge operation at 100 mA/cm<sup>2</sup> (a) with 0.1 g-Fe/cm<sup>2</sup> and (b) 10 g-Fe/cm<sup>2</sup>.

continues at a certain EMF corresponding to the gas composition achieved. As SOC decreases in proportion to the increase of the elapsed time, the amount of fresh reduced metal available for the hydrogen generation decreases. As Fig. 4.7 (a) clearly shows, the terminal voltage sharply decreases at a certain SOC in each current density. Under this SOC, high steam partial pressure is needed to enhance the metal oxidation reaction but it inevitably leads a sharp drop of EMF resulting in an insufficient operation of the battery. The sharp drop of the terminal voltage (EMF) is observed at a lower SOC for a higher current density.

The key phenomena in charge operation are the same as those in discharge operation discussed above, except for the opposite direction of the reactions. One noticeable difference is that the current density set in the calculations is low compared to that of discharge operation. To avoid a rapid degradation of the SOEC electrodes, the terminal voltage in charge operation should not be raised too high.

#### **4.2.5. Effects of amount of the redox metal**

From the battery concept, it is clear that the battery capacity is determined by the total amount of the redox metal in the system while the reaction rates are primarily controlled by the current density of the SOEC. Therefore the amount of the redox metal per unit surface area of the SOEC electrode is an important design parameter of the battery. Calculations were conducted varying the amount of the redox metal in the container. Figure 4.8 shows the distribution of  $\text{Fe}_3\text{O}_4$  ratio in discharge operation. Note that in Fig. 4.8 (a) and (b), the amount of the redox metal was set  $0.1 \text{ g/cm}^2$  and  $10 \text{ g/cm}^2$ , respectively. In this calculation, the initial porosity of reduced metal was

unchanged from the standard condition, 0.7. Variation of the redox metal amount also means that the length of the redox metal part,  $L_1$ , is varied. In Fig. 4.8 (a), the metal oxidation proceeds almost uniformly. It is ideal from the reaction point of view, because all the redox metal is effectively utilized. The low battery capacity, however, is an obvious penalty as a system. The case with  $10 \text{ g/cm}^2$ , the redox metal has a larger battery capacity but as shown in Fig. 4.8 (b) a significant delay of the redox reaction is observed at the inner part. This result shows that setting a suitable amount of the redox metal is a key to design this battery.

### 4.3. Summary

To understand the fundamental characteristics of a solid oxide redox flow battery, a gas-diffusion based time-dependent 1-D numerical simulation was conducted taking both the electrochemical and redox reactions into account. The electrochemical reaction rate at the SOEC is controlled by setting the current density as a boundary condition. Volume change of the redox metal is modeled as the change of local porosity and its effects on the gas diffusion is considered. Particular attention is paid to the distributions of the participating gas species, reaction rate, SOC and porosity in the porous redox metal. The following conclusions are obtained.

(1) Fundamental charge/discharge behavior of a solid oxide redox flow battery is numerically predicted. Reasonable and consistent results are obtained to discuss fundamental characteristics of the battery qualitatively.

(2) The balance of reaction rates between the metal redox reaction and the electrochemical reaction is an important factor. When two reactions equally proceed, the terminal voltage is almost constant and the system appears to be in a quasi-steady state. Under a condition in which the metal redox reaction becomes slow, the gas composition in the container shifts in a direction to lower the system performance. Because of this slow reaction, the terminal voltage quickly increases/decreases at the end of the charge/discharge operation.

(3) The gas diffusion in the redox metal needs to be carefully designed to ensure an effective reaction throughout the operation. At the beginning of the charge/discharge operation, the redox reaction is active near the surface region of the redox metal. The active region gradually moves to the inner region. The volume change of the redox

metal affects the effective diffusion coefficient and its effect is particularly important in discharge operation. The volume of the redox metal expands during the discharge operation leading reduction of the effective diffusion coefficient which limits the effective metal redox reaction. The large difference in spatial dispersion of the iron utilization might lead to both blocking of efficient consumption and promoting of partial degradation of iron, although it is considered that the gas diffusion is fast enough to maintain the battery performance.

## References

- [4.1] N. Xu, X. Li, X. Zhao, J. B. Goodenough, K. Huang, A novel solid oxide redox flow battery for grid energy storage, *Energy Environ. Sci.* 4 (2011) 4942-4946.
- [4.2] R. R. Melkote, K. F. Jensen, Computation of transition and molecular diffusivities in fibrous media, *AIChE Journal* 38 (1992) 56–66.
- [4.3] T. Suzuki, Z. Hasan, Y. Funahashi, T. Yamaguchi, Y. Fujishiro, M. Awano, Impact of anode microstructure on solid oxide fuel cells, *Science* 325 (2009) 852-855.

## **Chapter 5**

# **2-D numerical simulation of heat and mass transfer effects on SOIAB**

### **5.1. Numerical procedure**

#### **5.1.1. Battery design and computational domain**

Figure 5.1 schematically shows the configuration of the battery, which consists of an SOEC, the redox metal, a container, and an air channel. We set the  $x$ - and  $y$ -coordinates in the air flow direction and the SOEC thickness direction, respectively. For simplicity, we assume the system is long in  $z$ -direction (perpendicular to the  $x$ - $y$  plane) and focus only on the center region. That is, we assume uniform distribution of all values in  $z$ -direction and consider the phenomena are two-dimensional. We further simplify the air flow and the SOEC parts and we modeled each of these parts to be one dimensional in  $x$ -direction. The models are to be explained in the next section. The computational domain is marked with the red and blue broken line in Fig. 5.1. The

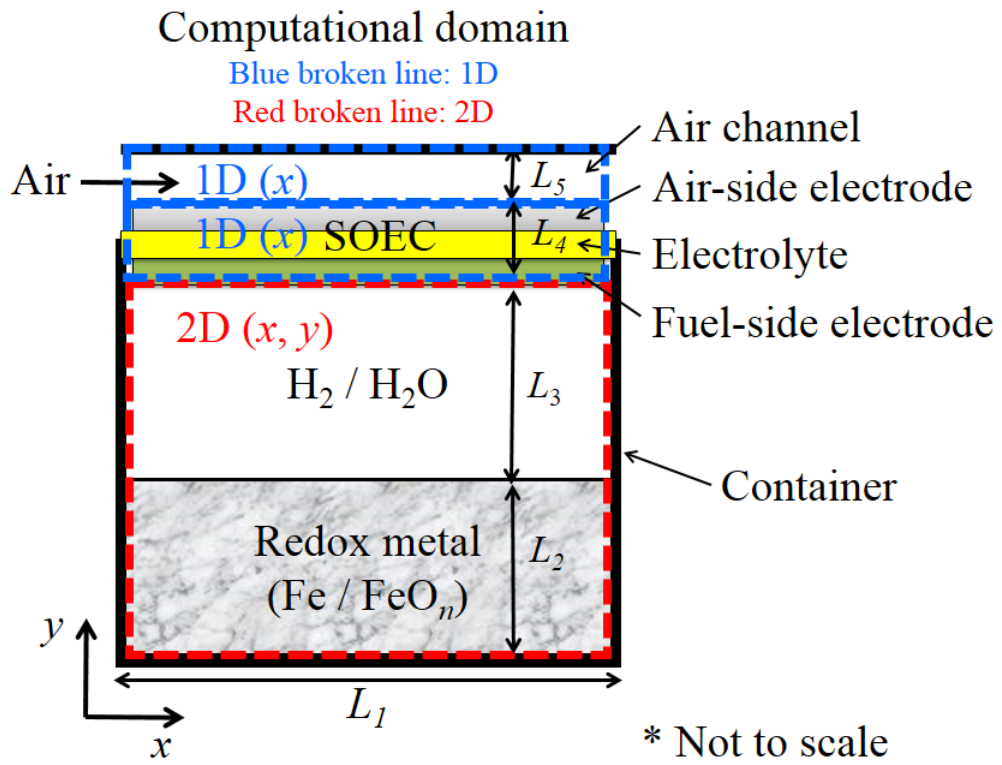


Figure 5.1. Schematic figure of the battery including the SOEC and the redox metal.

space inside the container is filled with the redox metal and the gaseous mixture of hydrogen and steam. As this space is isolated from the surrounding region and no external force is applied, the mass transfer inside the container is dominated by diffusion. The amount of the redox metal per unit area of the SOEC electrode is set at 1, 5, 10, or 20 g/cm<sup>2</sup>. The porosity of the redox metal is assumed to be 0.37 when it is fully oxidized.

For simplicity, the container wall is assumed to be very thin and that its heat capacity is negligibly small. The container is thermally insulated and, therefore, heat input to or heat release from the SOIAB occurs only through the heat exchange with the air flow, which is constantly supplied at a temperature of 550 °C. The depth of the redox metal ( $L_2$ ) is related to the amount of the redox metal per area in the SOEC electrode. 1 g/cm<sup>2</sup> of reduced redox iron results in  $L_2$  of 4.2 mm. Other design parameters of the system are as follows, length in  $x$ -direction,  $L_1=100$  mm, distance between redox metal and SOEC,  $L_3=10$  mm, thickness of the SOEC,  $L_4=1.0$  mm, and height of air channel,  $L_5=2.0$  mm.

### **5.1.2. Numerical modeling**

The computational domain shown in Fig. 5.1 is divided into two 1-D simulations and a 2-D simulation. They are all interrelated through the electrochemical reaction and heat transfer. The heat and mass generation/absorption caused by the reactions are considered as source terms. In 1-D simulations, the effects of heat transfer between the solid phase and gas phase appear as a source term as well.

### 5.1.2.1 1-D Simulation models for air flow and SOEC

As explained in the previous section, the air flow and the SOEC are treated as 1-D simulations in the  $x$ -direction, respectively. For the air flow, the mass and energy balances are considered neglecting the pressure drop along the channel.

$$\text{Mass:} \quad \frac{\partial \rho_a}{\partial t} + \frac{\partial(\rho_a u_a)}{\partial x} = S_{a, mass} \quad (5.1)$$

$$\text{Energy:} \quad \frac{\partial(\rho_a C_{p,a} T_a)}{\partial t} + \frac{\partial(\rho_a C_{p,a} u_a T_a)}{\partial x} = S_{a, heat} \quad (5.2)$$

where  $\rho_a$ ,  $C_{p,a}$  are mass density and specific heat of the binary mixture gas of nitrogen and oxygen flowing in the air channel.  $u_a$  is the velocity of the flow.  $T_a$ , and  $T_{SOEC}$  are the local temperature of the flow and the SOEC, respectively.  $S_{a, mass}$  and  $S_{a, heat}$  are source terms. Reflecting the oxygen consumption/generation by the electrochemical reaction,  $S_{a, mass}$  is calculated as  $\mp \frac{iM_{O_2}}{4F} \frac{1}{L_s}$ , where  $M_{O_2}$ ,  $F$  and  $i$  are the molecular weight of oxygen, Faraday constant and local current density. The sign is negative in discharge operation.  $S_{a, heat}$  is associated with the convective heat transfer between the flow and the SOEC. It is expressed as  $h(T_{SOEC} - T_a)/L_s$ .  $h$  is the heat transfer coefficient evaluated by assuming a constant Nusselt number of 4.86.

The SOEC is also treated as 1-D simulation in the  $x$ -direction. The energy equation is solved.

$$\text{Energy:} \quad \frac{\partial(\rho_{SOEC} C_{p,SOEC} T_{SOEC})}{\partial t} = \frac{\partial}{\partial x} \left( \lambda_{SOEC} \frac{\partial T_{SOEC}}{\partial x} \right) + S_{SOEC, heat} \quad (5.3)$$

where  $\rho_{SOEC}$ ,  $C_{p, SOEC}$ ,  $\lambda_{SOEC}$  are mass density, specific heat and thermal conductivity of the SOEC. Note that averaged values are used for these properties, evaluated

considering the materials and thicknesses of the electrodes and electrolyte. The source term,  $S_{SOEC, heat}$ , can be divided into three terms. The first term corresponds to the convective heat transfer between the air flow and the SOEC,  $h(T_a - T_{SOEC})/L_4$ . The second term corresponds to the heat exchange between the binary gas in the container and the SOEC,  $-\lambda_{gas}(\partial T_{gas}/\partial y)_{SOEC\ surface}/L_4$ .  $\lambda_{gas}$  is the thermal conductivity of the binary gas. The last term is the heat generation/absorption associated with the electrochemical reaction and the overpotentials in the SOEC and it is explained in the section 5.1.2.4.

### 5.1.2.2 2-D Simulation model in the container

A time-dependent 2-D numerical simulation based on energy and mass diffusion equations is conducted inside the container marked with the red broken line in Fig. 5.1. The 2-D simulation domain is further divided into two regions: the porous redox metal and the space between the SOEC and the redox metal. By choosing appropriate physical properties corresponding to each region, the governing equations can be written in the same form.

$$\text{Energy equation: } \frac{\partial(\rho C_p T)}{\partial t} = \frac{\partial}{\partial x} \left( \lambda \frac{\partial T}{\partial x} \right) + \frac{\partial}{\partial y} \left( \lambda \frac{\partial T}{\partial y} \right) + S_{heat} \quad (5.4)$$

$$\text{Mass transfer equation: } \frac{\partial Y_j}{\partial t} = \frac{\partial}{\partial x} \left( D \frac{\partial Y_j}{\partial x} \right) + \frac{\partial}{\partial y} \left( D \frac{\partial Y_j}{\partial y} \right) + S_{mass,j} \quad (5.5)$$

Where  $\rho$ ,  $C_p$ ,  $T$ ,  $\lambda$ ,  $S$ ,  $Y$ ,  $j$ ,  $D$  are mass density, specific heat, temperature, thermal conductivity, sources, concentration of species, species, and gas diffusion coefficient, respectively. Note that convection terms do not appear in these equations. Because of

the small characteristic length,  $L_3$ , and the temperature difference, the buoyancy force resulting from the variation in gas density cannot overcome the resistance caused by fluid viscosity, that is, the Rayleigh number is much smaller than its critical value. Natural convection does not occur under the calculation conditions set in this study and the gas transfer is governed by the diffusion process. Heat and mass generation associated with the reactions appear as source terms,  $S_{heat}$  or  $S_{mass, j}$  in the equations. They are explained in the sections 5.1.2.3 and 5.1.2.4

### **5.1.2.3 Redox reaction model of metal**

Although the redox reaction of iron involves complex elementary reactions, we simplified it to the overall reactions expressed by Eqs. 2.3 and 2.6 in this study. The reaction rates were obtained from a preliminary experiment using fine iron particles. Prior to the simulation, we performed thermogravimetry measurement for the iron particles supplying the mixture gas of hydrogen and steam. The exhaust gas composition was measured by using a mass spectrometry. The reaction rate is expressed in terms of the partial pressures of hydrogen and steam,  $p_{H_2}$  and  $p_{H_2O}$  and the molar density of the reactant,  $M_i$  in this study. The reactant is Fe in discharge operation while it is  $Fe_3O_4$  in charge operation. Note that not only  $p_{H_2}$  and  $p_{H_2O}$  but also  $M_i$  is a function of time and location since the reactant, Fe or  $Fe_3O_4$ , is consumed during the discharge and charge operations. The reaction rate is used to calculate the source terms. For example, the source term of Eq. 5.5 for hydrogen is evaluated using the local values of  $p_{H_2}$ ,  $p_{H_2O}$  and  $M_i$  as

Discharge:

$$S_{mass,H_2} = \left\{ - (k_1 \times P_{H_2}) + (k_2 \times P_{H_2O}) \right\} \times M_{Fe} \quad (5.6)$$

Charge:

$$S_{mass,H_2} = \left\{ - (k_1 \times P_{H_2}) + (k_2 \times P_{H_2O}) \right\} \times 3M_{Fe_3O_4} \quad (5.7)$$

where  $k_1$  and  $k_2$  are reaction coefficients. The values of reaction coefficients were evaluated by fitting the experimental data obtained by thermogravimetry measurement measurements. The temperature dependence of the reaction rates is also considered by changing the reaction coefficients in accordance with the temperature. Here, the rate is proportional to only the molar density of the reactant assuming that the activity of the solid phase (Fe or Fe<sub>3</sub>O<sub>4</sub>) is unity. When the operations proceed and Fe or Fe<sub>3</sub>O<sub>4</sub> is almost consumed up, the reaction rate decreases sharply and the discharge or charge operation comes to an end. The molar density of Fe,  $M_{Fe}$ , is related to the state of charge, SOC, which was explained in section 4.2.1, and is an important indicator of the battery condition. The SOC is explained in the latter section.

The reduced gas diffusion inside the porous metal was taken into account by considering an effective diffusion coefficient,  $D_{eff}$ . Here, we use the simple expression,  $D_{eff} = D_0 \times \varepsilon / \tau$ , where  $\varepsilon$  and  $\tau$  are the porosity and tortuosity factor of the porous material, respectively.  $D_0$  is the diffusion coefficient in a free space without porous material. The tortuosity factor is assumed to be the reciprocal of the porosity,  $\tau = 1 / \varepsilon$  [5.1].

We further assume that the representative pore diameter is much larger than the mean free path of hydrogen and we neglect Knudsen diffusion. The effective thermal conductivity of the porous region is modeled as  $\lambda_{eff} = \varepsilon \lambda_{gas} + (1 - \varepsilon) \lambda_{metal}$ . As we

assume iron to be the redox metal, its volume increases by a factor of 2.1 when it is oxidized. The volume expansion/shrinkage associated with the redox reaction is considered via the change in the local porosity of the redox metal. When the redox metal is fully reduced to Fe the porosity is 0.7 and when it is fully oxidized to Fe<sub>3</sub>O<sub>4</sub> the porosity is 0.37. It means that the  $D_{eff}$  discussed above takes a value in a range of  $0.14 \leq D_{eff} / D_0 \leq 0.49$ , depending on the local porosity.

Iron oxidation and reduction are exothermic and endothermic reactions, respectively. The reaction heat is evaluated from the enthalpy change,  $\Delta H$ , of Eqs. 2.3 and 2.6, respectively, considering its temperature dependency [5.2]. The local reaction rate is evaluated from the local  $p_{H_2}$ ,  $p_{H_2O}$ ,  $M_i$  and temperature and by considering the reaction heat,  $\Delta H$ , the local heat generation or absorption is obtained and is applied to the energy equation as a source term,  $S_{heat}$ .

#### 5.1.2.4 Reaction model at SOEC

There will be nonuniform distributions of the temperature and gas concentrations and, consequently, of the current density along the air-flow direction ( $x$ -direction) in the SOEC. In this simulation, the average current density is set at 200 mA/cm<sup>2</sup> and the terminal voltage is assumed to be uniform throughout the area, assuming high electric conductivity of the electrodes. The current is assumed to flow only in the thickness direction in the SOEC. The electromotive force,  $E$ , is locally evaluated by the Nernst equation,

$$E = E^0 + \frac{RT}{2F} \ln \left( \frac{p_{H_2} \times p_{O_2}^{1/2}}{p_{H_2O}} \right) \quad (5.8)$$

$$E^0 = \frac{\Delta G^0}{2F} \quad (5.9)$$

where  $E^0$ ,  $R$ ,  $F$ , and  $\Delta G$  are the standard electromotive force, gas constant, Faraday constant and Gibbs free energy change, respectively. The concentration overpotential is neglected. The IR loss,  $\eta_{ohm}$ , is expressed as  $\eta_{ohm} = ASR_{ohm} * i$ , where  $i$  and  $ASR_{ohm}$ , are the local current density and area-specific resistance, respectively.  $ASR_{ohm}$  was set to be  $1e-5$  [ $\Omega m^2$ ] by fitting to an  $i$ - $V$  curve obtained from an experiment performed at  $600$  °C [5.3] and was assumed to be constant. The activation overpotential,  $\eta_{act}$ , is evaluated by a Butler-Volmer type equation [5.4]

$$i = i_0 \left[ \exp\left(\frac{2F\eta_{act}}{RT}\right) - \exp\left(\frac{-F\eta_{act}}{RT}\right) \right] \quad (5.10)$$

The exchange current density,  $i_0$ , is generally a function of local temperature and gas concentrations. In this study, however, its value is assumed to be constant at a value estimated at  $600$  °C [5.3]. It is still difficult to find conclusive experimental data available that cover both hydrogen oxidation and steam electrolysis using practically same cells under low temperature condition set in this study,  $500 - 650$  °C. Then the terminal voltage,  $V$ , can be obtained as

$$\text{Discharge :} \quad V_{\text{discharge}} = E - (\eta_{ohm} + \eta_{act}) \quad (5.11)$$

$$\text{Charge :} \quad V_{\text{charge}} = E + (\eta_{ohm} + \eta_{act}) \quad (5.12)$$

The generation/consumption of oxygen associated with the electrochemical reaction on the air-electrode is included in the calculation as a source term (see section 5.1.2.2). The generation/consumption of hydrogen or steam associated with the electrochemical reactions on the fuel-side electrode are also included in the calculation as a boundary condition at the surface of the electrode. It is introduced to the calculation

as a source term of the gas-phase grid adjacent to the SOEC electrode. They are evaluated from the local current density as shown in Table 5.1.

The hydrogen oxidation in discharge operation and the steam electrolysis reaction in charge operation at the SOEC are exothermic and endothermic, respectively. In these reactions, the thermal energy associated with  $T\Delta S$  of Eqs. 2.2 or 2.5 is released or absorbed.  $\Delta S$  is the entropy change of the reaction. The local reaction rate is obtained from the local current density and by considering  $T\Delta S$ , the heat generation or absorption is calculated and is included in the source term of the energy equation of the SOEC,  $S_{\text{SOEC}, \text{heat}}$  of Eq. 5.3. In addition to this, there are heat generation caused by inner resistance and activation overpotential during both hydrogen oxidation and steam electrolysis. The heat generation associated with Joule heating,  $i^2 \times ASR_{ohm}$ , and activation overpotential,  $i \times \eta_{act}$ , are also included in the source term of the energy equation of the SOEC,  $S_{\text{SOEC}, \text{heat}}$  of Eq. 5.3.

### 5.1.2.5 Numerical procedure

An in-house program code was applied to the battery model shown in Fig. 5.1. The governing equations were discretized using the finite volume method. A nonuniform grid system was applied with finer grid spacing in the porous redox metal medium, where a steep concentration gradient was expected. A fully implicit method was used to solve Eqs. 5.4 and 5.5. The time increment was set at 0.2 s for the iron density of 1 g/cm<sup>3</sup>. A systematic test was conducted to confirm that the results were independent of the grid or time increment. The boundary conditions for Eqs. 5.4 and 5.5

are summarized in Table 5.1 and Table 5.2. Note that the effects of the electrochemical and redox reactions are taken into account through the source terms

### 5.1.2.6 Computational conditions

We conduct two types of calculations in this study. The first type is conducted for a noncyclical simple discharge/charge operation to determine the fundamental characteristics of the system. The redox metal is completely reduced/oxidized at the beginning of the discharge/charge operation and set as the initial condition. As we defined in section 4.2.1, the state of charge, SOC is the ratio of the capacity stored in the battery to that at full charge. It is evaluated based on the molar density of Fe. At an extreme condition when the battery is fully charged, all iron exists as Fe. If we write the molar density of Fe at this condition as  $M_{Fe}^0$ , the local SOC during the operation can be expressed as  $M_{Fe}/M_{Fe}^0$  using the instantaneous value of  $M_{Fe}$  at each location. The battery's total SOC can be calculated taking the average of the local SOC. The SOC is 100% when the battery is fully charged. Because the current density is kept constant in each operation, the elapsed time is proportional to SOC.

After the single discharge/charge calculations, a calculation of the discharge/charge cycle operations is conducted. SOC is set at 100% as the initial condition. When SOC reaches 50% in the first discharge operation, the operation mode is switched to the charge operation and the battery is charged until SOC reaches 98%.

Table 5.1. Mass generation rates of species by the electrochemical reactions [ $\text{kg}\cdot\text{m}^{-3}\text{ s}^{-1}$ ].

Position	SOEC Operation	$S_{mass,j}$	
		H <sub>2</sub>	H <sub>2</sub> O
Computational grid adjacent to fuel-side electrode of SOEC	Discharge	$-\frac{M_{\text{H}_2}}{2F} \frac{i}{\Delta y}$	$\frac{M_{\text{H}_2\text{O}}}{2F} \frac{i}{\Delta y}$
	Charge	$\frac{M_{\text{H}_2}}{2F} \frac{i}{\Delta y}$	$-\frac{M_{\text{H}_2\text{O}}}{2F} \frac{i}{\Delta y}$

$\Delta y$ : Grid size in  $y$  direction,  $M_j$ : Molecular weight of species

Table 5.2. Boundary conditions.

	$T$	$Y_j$
Fuel-side electrode of SOEC	$\lambda_{gas} \frac{\partial T_{gas}}{\partial y} \Big _{\text{interface}} = \lambda_{solid} \frac{\partial T_{solid}}{\partial y} \Big _{\text{interface}}$	$\frac{\partial Y_j}{\partial y} = 0$
Side walls ( $x=0, 100$ mm)	$\frac{\partial T}{\partial x} = 0$	$\frac{\partial Y_j}{\partial x} = 0$
Bottom wall ( $y=0$ mm)	$\frac{\partial T}{\partial y} = 0$	$\frac{\partial Y_j}{\partial y} = 0$

The discharge and charge operations are sequentially repeated three times with SOC varied between 50% and 98%.

In both calculations, the system is initially set at 550 °C with a total pressure of 1 atm. The SOEC is operated in a constant-current mode. At the inlet of the air channel, dry air ( $N_2 : O_2 = 79 : 21$ ) is supplied at a constant temperature of 550 °C. The inlet velocity of the air flow is fixed at 1.84 m/s. It corresponds to the oxygen utilization factor of 5% in the discharge operation. Note that the air flow plays an important role in maintaining the system temperature within a certain limit. Because the air inlet temperature is kept constant, the air acts as coolant when there is excess heat generation in the system, while it acts as a heat supply when there is insufficient heat in the system.

## 5.2. Results and discussion

### 5.2.1. Fundamental characteristics under discharge/charge operations

Figure 5.2 shows the operation curves, i.e., the terminal voltage as a function of capacity density, under charge/discharge conditions for various iron densities. The iron density is the amount of iron per unit area of the SOEC electrode. The thickness of the redox metal in the container,  $L_2$ , is proportional to the iron density.  $L_2$  is 4.2, 21, 42 and 82 mm for iron density 1, 5, 10 and 20 g/cm<sup>2</sup>, respectively. Note that the capacity density is proportional to SOC or (1-SOC) since SOC is the normalized capacity. The capacity is also proportional to the elapsed time because the current density is kept constant, although each iron density has a different elapsed time. The operation time is approximately 6.5 h for an iron density of 1 g/cm<sup>2</sup>.

Comparing the discharge and charge operations, the terminal voltage under the charge operation is naturally higher than that under the discharge operation. For each operation, sharp changes are observed in the last part above a capacity density of 1200 mAh/g-Fe. This reflects the limited reaction of the redox metal since there is little usable redox metal remaining at this stage. In the discharge operation, the terminal voltage is lower at a higher iron density for the same SOC. The situation is opposite in the charge operation; the terminal voltage is higher for a higher iron density. The difference of the terminal voltage for different iron density is related to its temperature and gas diffusion in the container, which are discussed in latter sections.

It was shown that the discharge and charge operations produce similar results, although their tendencies are almost opposite. Therefore, the results of the discharge

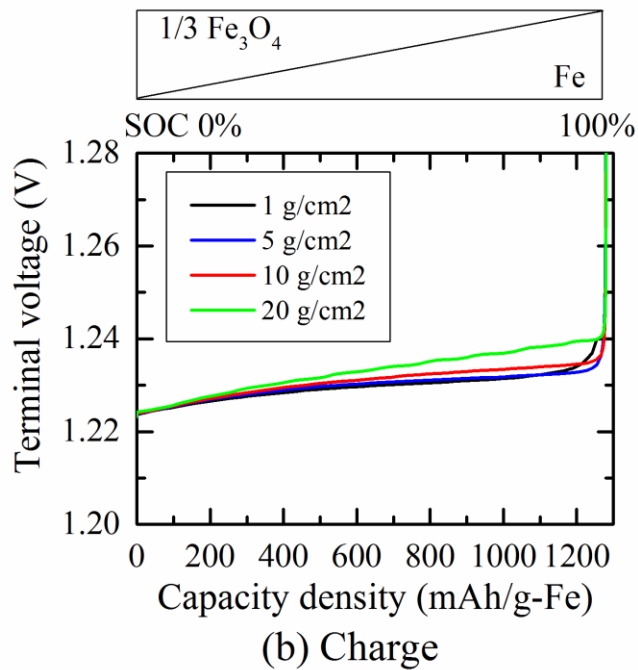
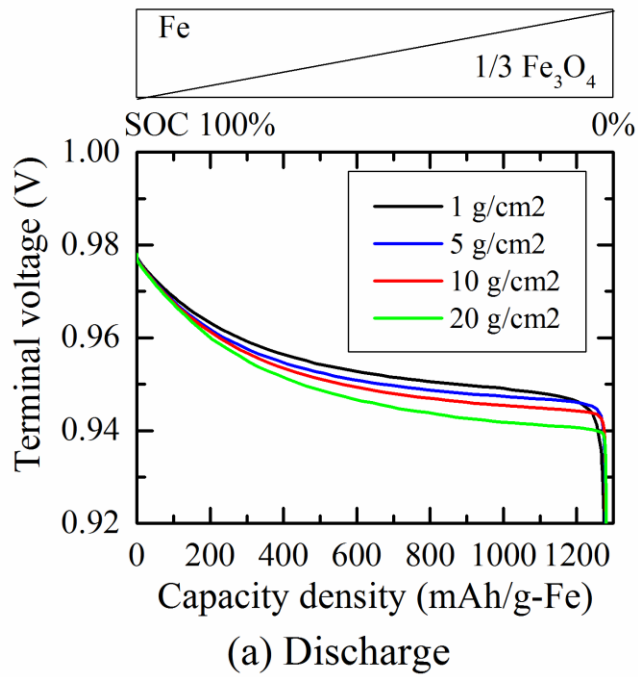


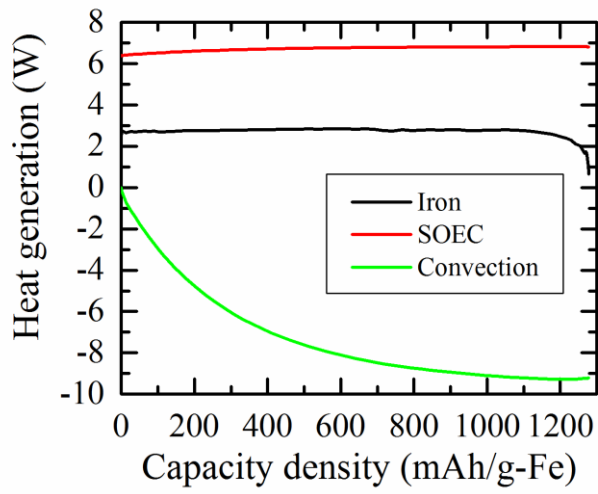
Figure 5.2. Operation curves in (a) discharge operation and (b) charge operation with iron densities of 1, 5, 10, and 20 g/cm<sup>2</sup>.

operation are discussed first hereafter, followed by those of the charge operation, although graphs of both operations are shown next to each other in some figures.

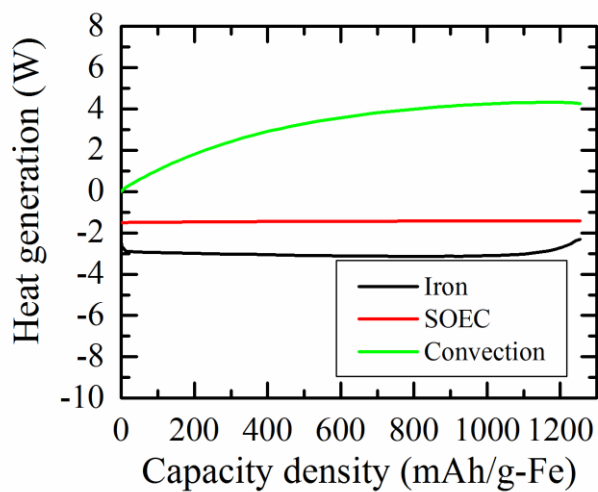
### **5.2.2. Heat transfer during discharge operation**

In the discharge operation, the oxidation of iron and the power generation reactions in the SOEC are exothermic reactions generating heat. The generated heat is removed from the system by the convective heat transfer between the air flow and the SOEC. This means that the air functions not only as the oxygen supply for the electrochemical reaction but also as the coolant of the system. The thermal budget during the discharge operation is shown in Fig. 5.3 (a) for an iron density of 1 g/cm<sup>2</sup>. In the figure, a negative value implies heat removal from the system. Heat generation from the SOEC and the redox metal is almost constant under the constant-current operation adopted in this study. In contrast, the amount of heat exchanged between the battery and the air flow through convective heat transfer increases as time elapses. The figure shows that the cooling effect of the air flow is not sufficient particularly at the beginning of the operation.

The changes in the average temperatures of the SOEC and the redox metal corresponding to Fig. 5.3 (a) are shown in Fig. 5.4 (a). The average temperature rises by about 50 °C during the discharge operation. The temperature rise is steep at the beginning of the operation when the temperatures of the SOEC and the redox metal are relatively low. Since the air inlet temperature is kept constant in these calculations, the temperature

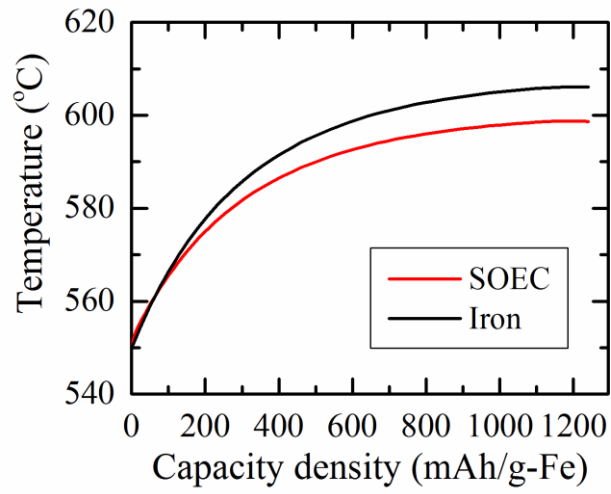


(a) Discharge

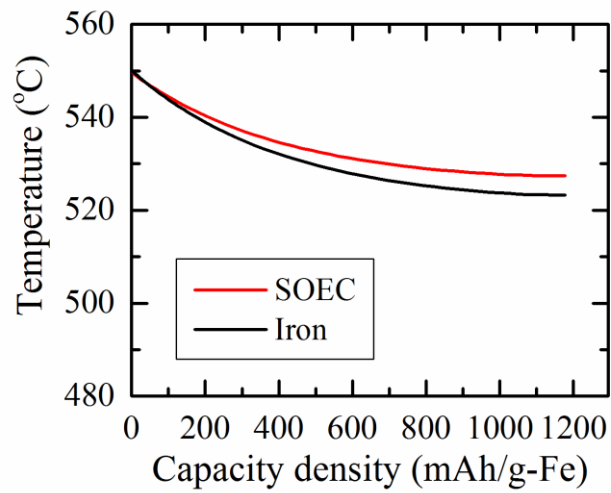


(b) Charge

Figure 5.3. Heat generation balance of the system including both reaction heat and convectional heat in (a) discharge operation and (b) charge operation with iron density of  $1 \text{ g/cm}^2$ .



(a) Discharge



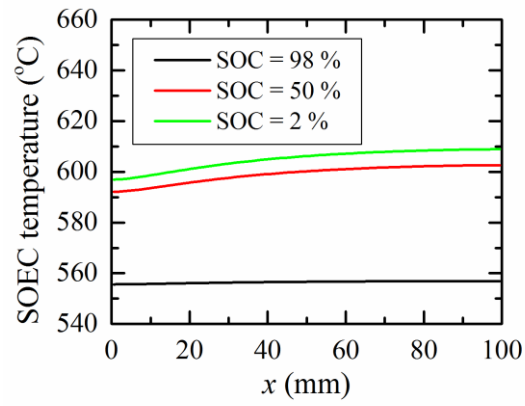
(b) Charge

Figure 5.4. Temperature changes in (a) discharge operation and (b) charge operation with iron density of  $1 \text{ g/cm}^2$ .

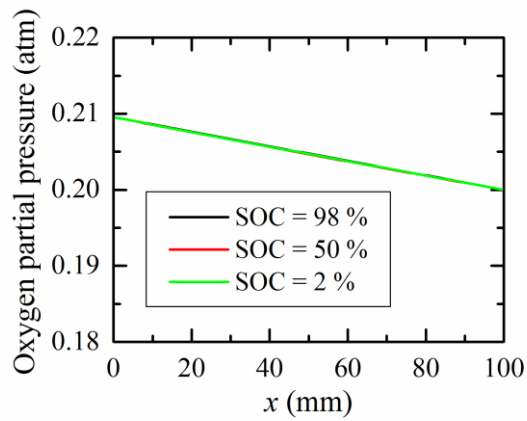
difference between the air flow and the SOEC is relatively small at the beginning of the operation, which limits the cooling effect of the air. As a result, there is a large amount of excess heat generation that leads to a rapid temperature rise. As time elapses, the average temperature of the SOEC increases, increasing the temperature difference between the air flow and the SOEC. This enhances the cooling effect of the air as shown in Fig. 5.3 (a) and the gradient in Fig. 5.4 (a) becomes gradually small as time elapses.

### **5.2.3. Current density distribution of SOEC during discharge operation**

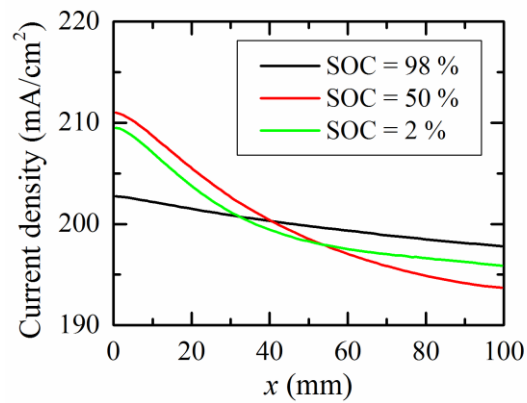
The distributions of the SOEC local temperature, the oxygen partial pressure in the air flow, and the local current density along the air flow direction ( $x$ -direction) are shown in Fig. 5.5 for an iron density of  $1 \text{ g/cm}^2$  at SOC of 2, 50, and 98%. Fig. 5.5 (a) shows that the local temperature profile is relatively uniform, particularly at the beginning of the discharge operation (SOC = 98%) and increases almost uniformly as time elapses. In the upstream region, where the SOEC is exposed to fresh air, temperature is relatively lower. The temperature difference along the  $x$ -direction is approximately  $12 \text{ }^\circ\text{C}$  at SOC = 2%. The oxygen partial pressure decreases along the air flow direction, as shown in Fig. 5.5 (b), although the hydrogen partial pressure is almost uniform along the SOEC (not shown). The local current density is higher in the upstream region as shown in Fig. 5.5 (c). The slope of the local current density is steep in the upstream region for SOC = 50% and 2%. This is attributed to the above-mentioned temperature distributions. At high temperatures, the activation overpotential is lower and the system becomes more



(a) SOEC temperature



(b) Oxygen partial pressure



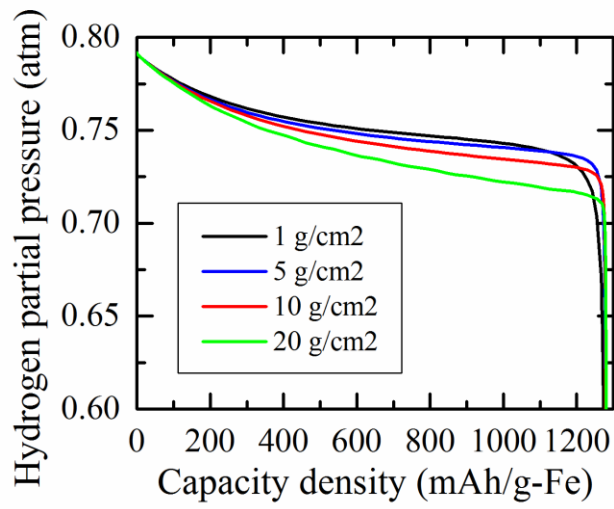
(c) Current density

Figure 5.5. Distributions along air flow of (a) temperature of SOEC, (b) oxygen partial pressure in air flow, and (c) current density of SOEC in discharge operation with iron density of  $1 \text{ g/cm}^2$ .

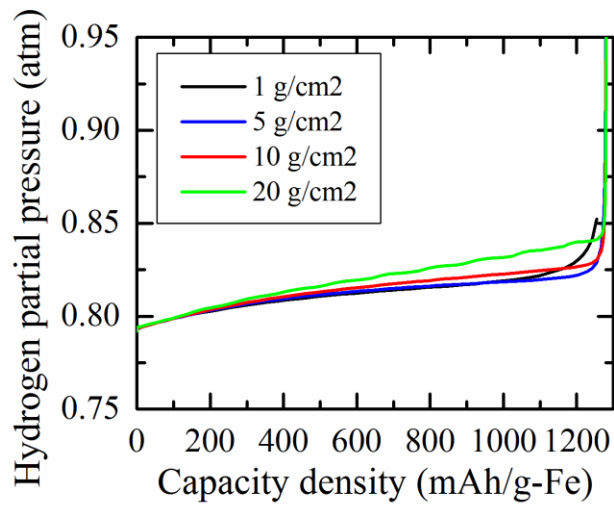
sensitive to the EMF. Because of the relatively low temperature in the upstream region, the EMF is higher in this region, resulting in a higher local current density. The difference in the local current density between the upstream and downstream is about 9%. Although the local temperature profile is relatively uniform with a maximum difference of approximately 12 °C in this study, it has a clear effect on the local current density distribution.

#### **5.2.4. Evolution of redox reaction area during discharge operation**

The hydrogen partial pressure during the discharge operation is shown in Fig.5.6 (a) for four cases with different iron densities. It is an average value of the hydrogen partial pressure in the free diffusion space between the SOEC and redox metal. As the temperature rises (Fig. 5.4 (a)), the equilibrium partial pressure of hydrogen decreases since the metal oxidation reaction is exothermic (Eq. 2.3). On the other hand, the hydrogen partial pressure must be slightly below the equilibrium pressure during the discharge operation so that the redox metal can supply sufficient hydrogen. Then, the hydrogen partial pressure decreases with time as shown in Fig. 5.6 (a), following the decrease in the equilibrium pressure. Note that the difference between the hydrogen partial pressure and the equilibrium pressure depends on the balance between the electrochemical reaction at the SOEC and the redox reaction. If the redox reaction is slow and the hydrogen generation rate is insufficient to replace the hydrogen consumed by the SOEC, the hydrogen partial pressure drops and the difference from the



(a) Discharge

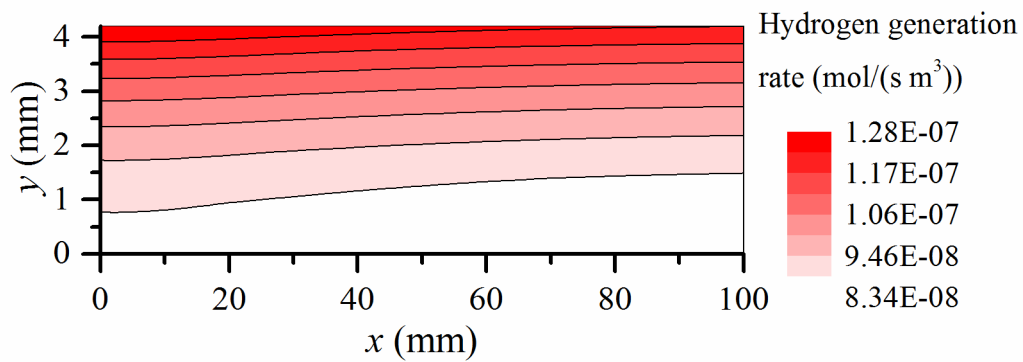


(b) Charge

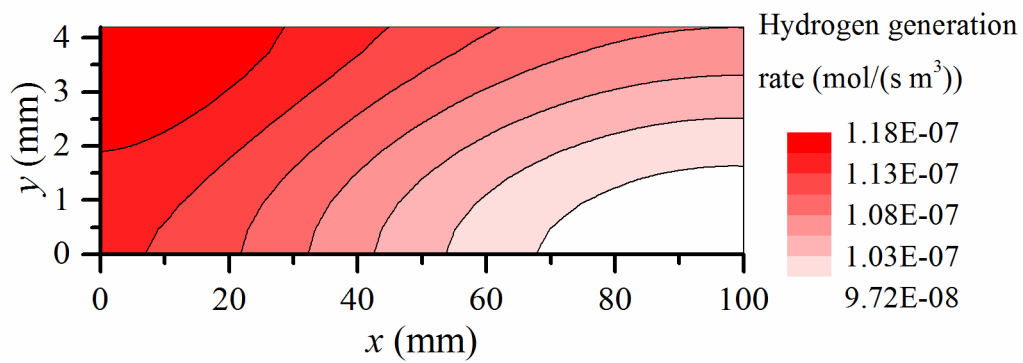
Figure 5.6. Change in hydrogen partial pressure in (a) discharge operation and (b) charge operation with iron densities of 1, 5, 10, and 20 g/cm<sup>2</sup>.

equilibrium pressure becomes large. This enhances the redox reaction to generate more hydrogen. In contrast, if the redox reaction is sufficiently fast, the hydrogen partial pressure remains close to the equilibrium pressure. These tendencies correspond well with those in another experiment that we performed (not published). At the end of the operation, when little fresh iron remains, the hydrogen partial pressure sharply drops as shown in Fig. 5.6 (a). This is consistent with the sharp drop in the terminal voltage observed in Fig.5.2 (a).

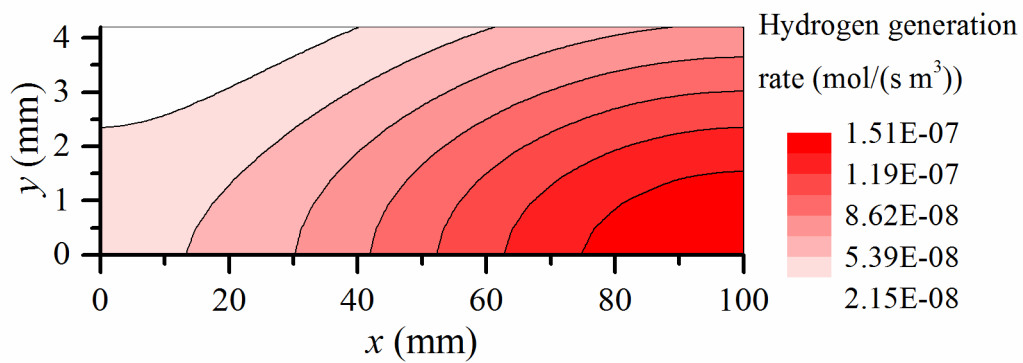
In Fig. 5.6 (a), the hydrogen partial pressure is generally lower for a higher iron density. It is a combined effect of the temperature and gas diffusion. In addition to the above mentioned change of the equilibrium pressure due to the temperature, the gas diffusion affects the gas composition near the SOEC and consequently, the EMF. To observe its effects, the distributions of the local hydrogen generation rate in the redox metal and the local SOC are first examined in this section for an iron density of  $1 \text{ g/cm}^2$  as shown in Figs. 5.7 and 5.8, respectively. Note that only the redox metal region is depicted in these figures. Metal oxidation first proceeds actively near the surface approximately  $3 \text{ mm} < y < 4 \text{ mm}$  as shown in Fig. 5.7 (a). Then, reflecting the higher local current density in the upstream shown in Fig. 5.5 (c), the main active area is the upstream region of approximately  $0 \text{ mm} < x < 20 \text{ mm}$  (Fig. 5.7 (b)). The local SOC shown in the corresponding figures (Figs. 5.8 (a) and (b)) indicates the ratio of fresh iron. It is clearly shown that after the fresh iron near the upstream surface region is consumed, the active area shifts to the bottom downstream region, where a large amount of iron remains (Figs. 5.7 (c) and 5.8 (c)). It makes the gas diffusion path in the redox metal longer. Because the diffusion resistance increases, the gas composition in the



(a) SOC = 98 %

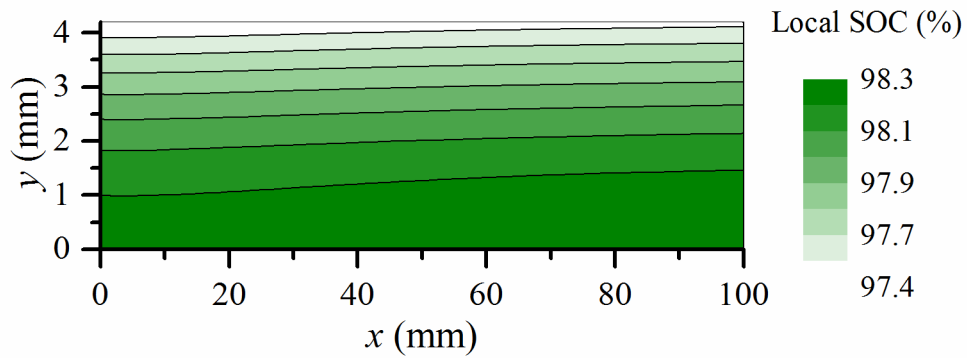


(b) SOC = 50 %

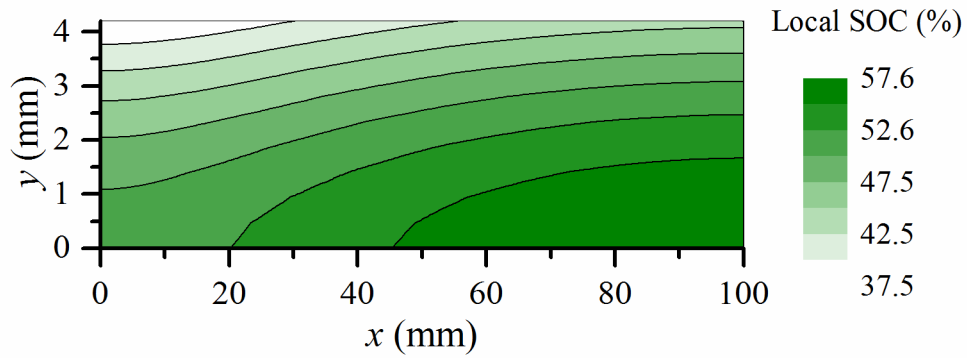


(c) SOC = 2 %

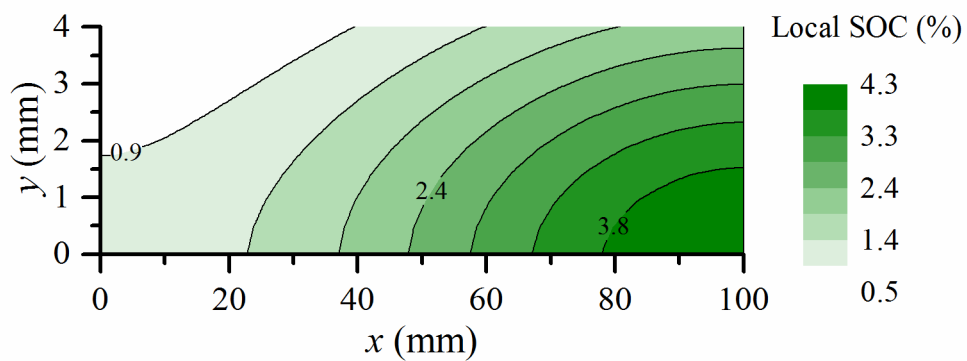
Figure 5.7. Distributions of hydrogen generation rate in the redox metal region in discharge operation at (a) SOC = 98%, (b) SOC = 50%, and (c) SOC = 2% with iron density of 1 g/cm<sup>2</sup>.



(a) SOC = 98 %



(b) SOC = 50 %



(c) SOC = 2 %

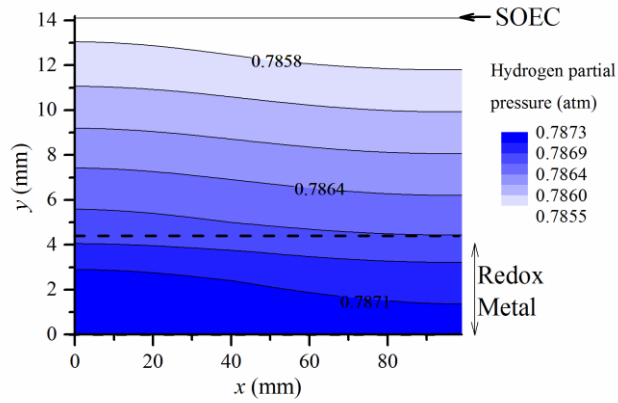
Figure 5.8. Distributions of local SOC in the redox metal region in discharge operation at (a) SOC = 98%, (b) SOC = 50%, and (c) at SOC = 2% with iron density of 1 g/cm<sup>2</sup>.

space between the SOEC and the redox metal shifts to steam-rich composition. The gas diffusion effect is discussed in the next session.

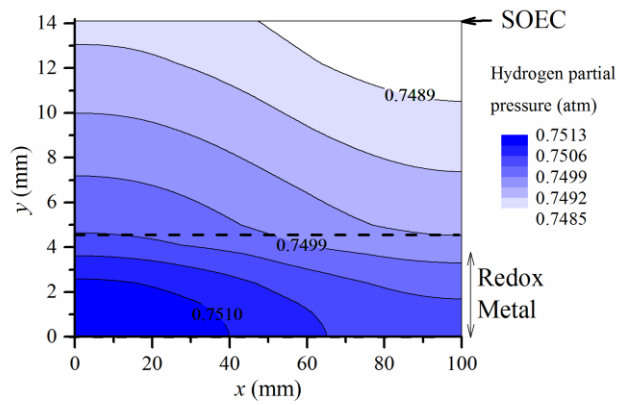
### **5.2.5. Gas diffusion during discharge operation**

Figure 5.9 shows the evolution of the distribution of local hydrogen partial pressure for an iron density of  $1 \text{ g/cm}^2$ . Note that this figure covers not only the redox metal region but also the space between the redox metal and the SOEC electrode. When the metal is oxidized, it expands and the local porosity decreases. The nonuniform local porosity and its evolution inevitably affect the effective gas diffusion coefficient in the porous metal region. These effects are taken into account in the calculations. At SOC = 98%, hydrogen is generated near the surface of the redox metal as shown in Figs. 5.7 (a) and 5.10 (a). Because of the uniform hydrogen production in the  $x$ -direction, the gas diffusion can be approximated as 1-D diffusion in the positive  $y$ -direction. Note that because of the redox reaction, the local porosity of the redox metal becomes lower near the surface at the beginning of the discharge process. The low-porosity region formed near the surface acts as a barrier layer to reduced gas diffusion. At SOC = 50%, shown in Fig. 5.9 (b), the hydrogen generation is active in the upstream region. The generated hydrogen is supplied to the SOEC by diffusion while some of the hydrogen is trapped in the bottom region of the redox metal. This is because the resistance to diffusion near the redox surface is relatively high owing to the low porosity mentioned above. At SOC = 2%, the hydrogen generation is only active in the bottom downstream region in the redox metal. The supply of hydrogen from only this region results in the contour map shown in Fig. 5.9 (c), which is very different from that in Fig. 5.9 (a). Reflecting the

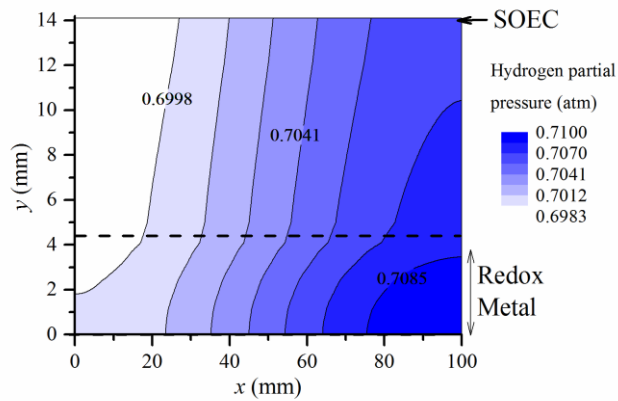
reduced gas diffusion in the redox metal region ( $0 \text{ mm} < y < 4 \text{ mm}$ ), the gradient is steep in this area. In Fig. 5.9 (c), if we calculate the gradient in  $y$ -direction at  $x = 90 \text{ mm}$ ,  $y = 3 \text{ mm}$  (inside of the porous metal), its value is 7 times larger than that calculated at  $x = 90 \text{ mm}$ ,  $y = 5 \text{ mm}$  (outside of the porous metal).



(a) SOC = 98 %



(b) SOC = 50 %



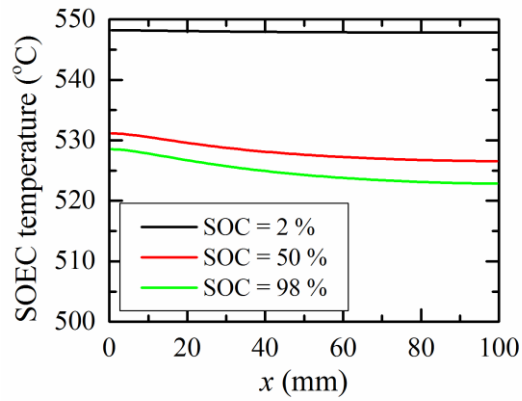
(c) SOC = 2 %

Figure 5.9. Distribution of hydrogen partial pressure in the container in discharge operation at (a) SOC = 98%, (b) SOC = 50%, and (c) at SOC = 2% with iron density of 1 g/cm<sup>2</sup>.

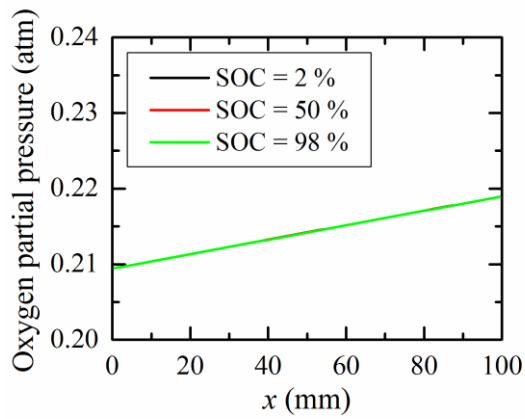
Although there is a clear difference in the gradient reflecting the difference of the effective diffusion coefficient, the distribution of the hydrogen partial pressure can generally be regarded as uniform for an iron density of  $1 \text{ g/cm}^2$  shown in Fig. 5.10. Its non-uniformity increases when the iron density is higher because the redox metal thickness,  $L_2$ , is longer. The maximum difference of the hydrogen partial pressure observed at SOC=50% and 2% for iron density of  $20 \text{ g/cm}^2$  was 0.025 and 0.043 atm that correspond to around 5 and 8 mV of EMF, respectively. It means if the gas diffusion is effectively enhanced in the redox metal region, its terminal voltage shown in Fig. 5.2 (a) can be improved to take a closer value of the iron density of  $1 \text{ g/cm}^2$ . The insufficient gas diffusion in the redox metal also causes another and probably severer problem of a non-uniform utilization of the redox metal. Its effect will be more prominent under high iron density condition and is to be discussed in section 5.2.7.

### **5.2.6. Charge operation**

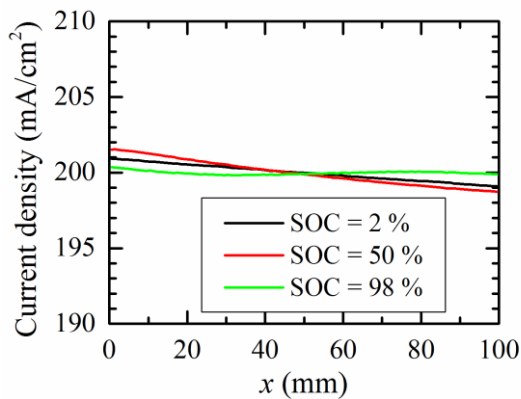
The phenomena observed during the charge operation can generally be understood as the result of reverse reactions to those occurring in the discharge operation. As shown in Fig. 5.3 (b), the heat absorption resulting from the reduction of iron oxide and the electrochemical reaction is almost constant during the operation. Note that the SOEC operates below the thermal neutral point owing to the relatively low current density assumed in this study. The heat supplied by the air is insufficient to maintain the temperature of both the SOEC and the redox metal (Fig. 5.4 (b)). Their average temperatures continue to decrease during the operation and never reach a thermal steady



(a) SOEC temperature



(b) Oxygen partial pressure



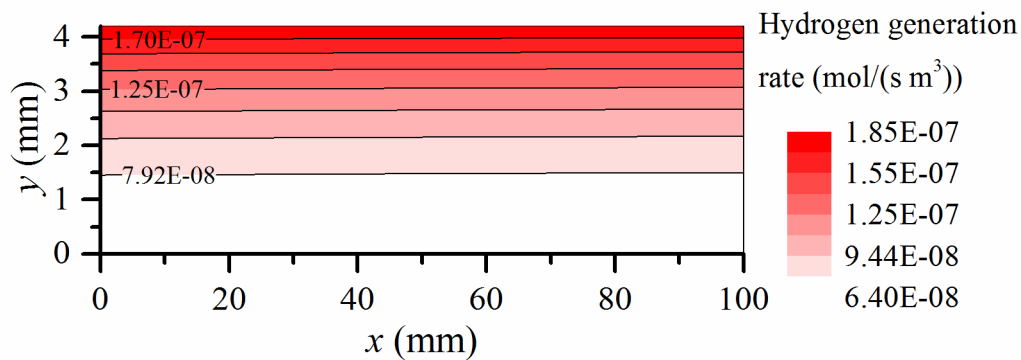
(c) Current density

Figure 5.10. Distributions along air flow of (a) temperature of SOEC, (b) oxygen partial pressure in air flow, and (c) current density of SOEC in charge operation with iron density of  $1 \text{ g/cm}^2$ .

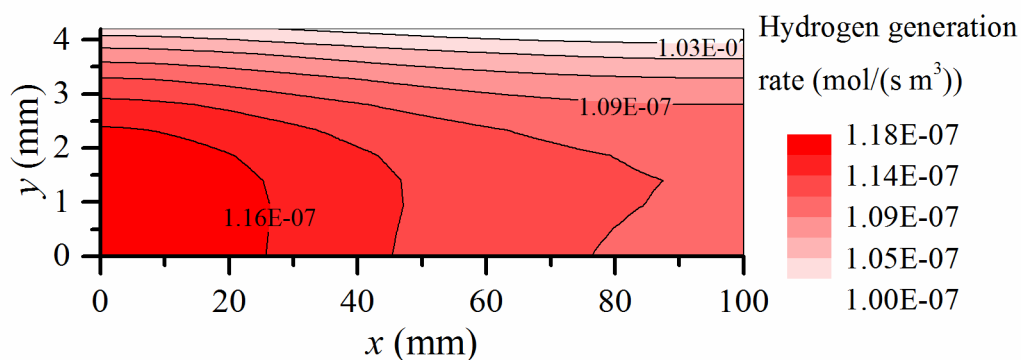
state. It is worth noting that the heat generation caused by the internal losses of the SOEC can be effectively utilized to the endothermic reactions during the charge operation, not only for the steam electrolysis but also for the reduction of  $\text{Fe}_3\text{O}_4$ . If the current density is high and heat generation from the SOEC is sufficient, there will be no need for additional heat supply from outside of the system.

The distributions of the SOEC local temperature, the oxygen partial pressure in the air flow, and the local current density along the  $x$ -direction during the charge operation are shown in Fig. 5.10, which correspond to those in Fig. 5.5 for the discharge operation. There is a noticeable difference in the local current density distribution for the charge and discharge operations (Figs. 5.10 (c) and 5.5 (c)). In the charge operation, the local current density remains relatively flat. As the temperature decreases, a higher EMF is expected while the activation overpotential also increases. The current density distribution is determined as a result of the trade-off between these two effects.

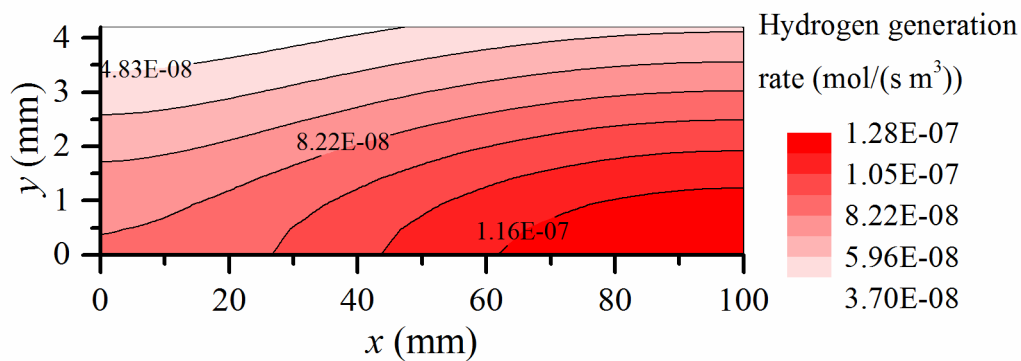
The temporal change in the hydrogen partial pressure shown in Fig. 5.6 (b) is consistent with the time course of the temperature shown in Fig. 5.4 (b). Figure 5.6 (b) also shows that the dependence of the hydrogen partial pressure on the iron density is similar to that in the discharge operation. The distributions of the local hydrogen absorption rate and local SOC are examined for an iron density of  $1 \text{ g/cm}^2$  as shown in Figs. 5.11 and 5.12, respectively. Note that only the redox metal region is depicted in these figures. The active reaction area in the redox metal gradually shifts in a similar manner to that in the discharge operation. When iron oxide is reduced, it shrinks and the local porosity increases, increasing the rate of gas diffusion. This is a clear difference



(a) SOC = 2 %

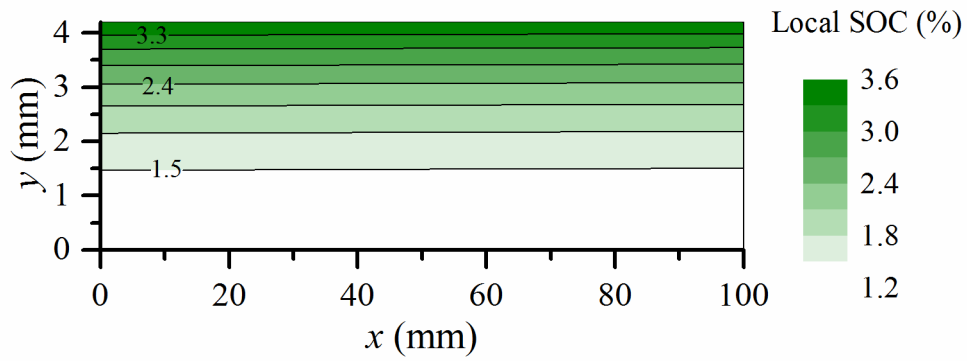


(b) SOC = 50 %

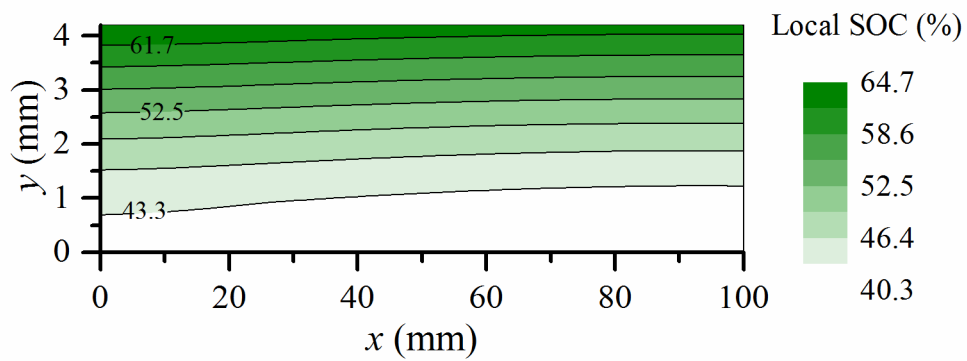


(c) SOC = 98 %

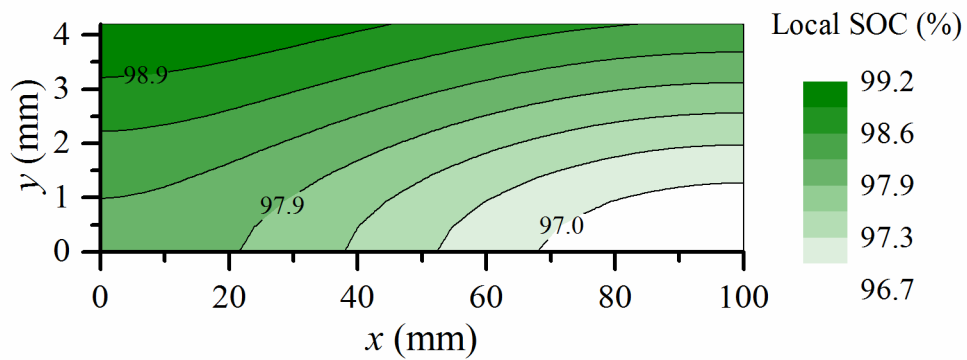
Figure 5.11. Distributions of hydrogen absorption rate in the redox metal region in charge operation (a) at SOC = 2%, (b) at SOC = 50%, and (b) at SOC = 98% with iron density of 1 g/cm<sup>2</sup>.



(a) SOC = 2 %



(b) SOC = 50 %



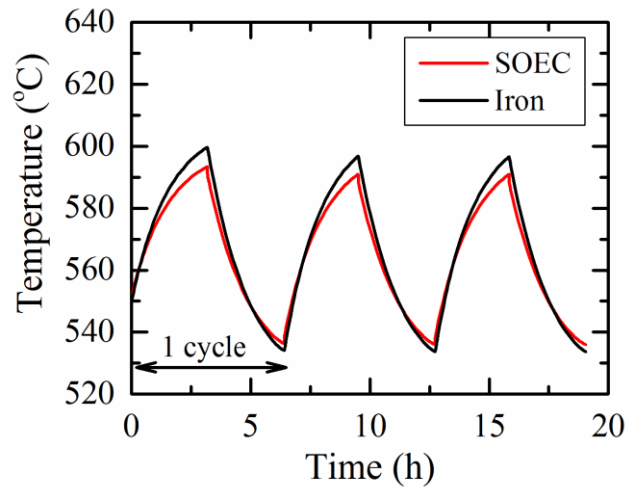
(c) SOC = 98 %

Figure 5.12. Distributions of local SOC in the redox metal region in charge operation (a) at SOC = 2%, (b) at SOC = 50%, and (b) at SOC = 98% with iron density of 1 g/cm<sup>2</sup>.

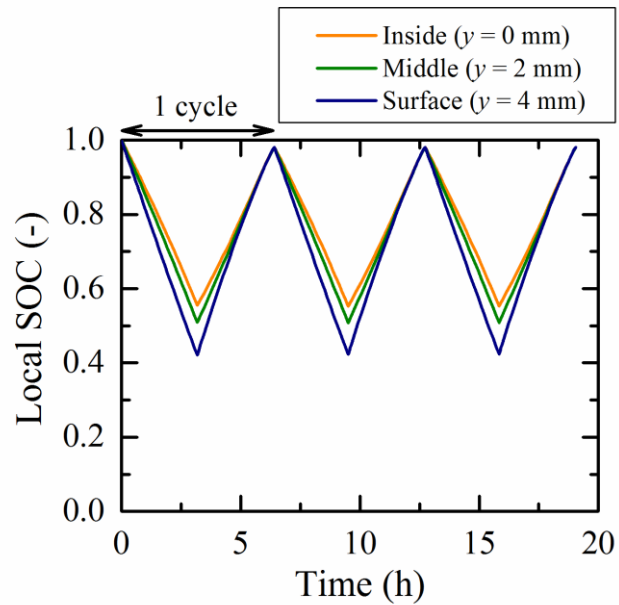
between the discharge operation and the charge operation as follows. In the discharge operation a barrier layer is formed near the surface region by the volume expansion of iron, while in the charge operation the gas diffusion is enhanced as the iron oxide is reduced. The active area moves to the inner region of the redox metal more rapidly in the charge operation. The evolution of the local SOC progresses almost uniformly as shown in Fig. 5.12 (b).

### **5.2.7. Discharge/charge cycle operation**

The discharge/charge cycle operation was calculated with iron densities of 1 and 5 g/cm<sup>2</sup>. SOC is set at 100% at the beginning of the calculation. When SOC reaches 50% in the first discharge operation, the operation mode is switched to the charge operation and the battery is charged until SOC reaches 98%. The discharge and charge operations are sequentially repeated three times with SOC varied between 50 and 98%. Figures 5.13 and 15 show the time courses of the temperature and SOC for iron densities of 1 and 5 g/cm<sup>2</sup>, respectively. In the cycle operation, the temperature rises in the discharge operations and decreases in the subsequent charge operations as shown in Figs.5.13 (a) and 5.14 (a). As a result, the system temperature remains in a certain range without using any additional heating or cooling devices except for the air flow supplied at a constant temperature. During the cycle operation under calculation condition in this study, some of the heat released in the discharge operation is stored as a temperature increase in the battery itself and is utilized in the charge operation. In other words, the battery body is used as a thermal storage in this case.

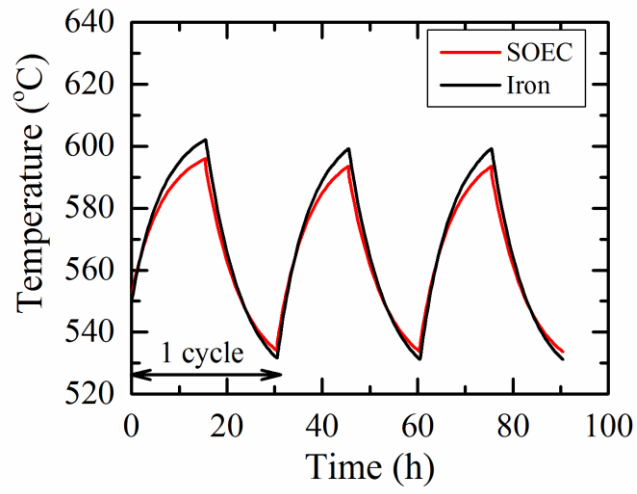


(a) Temperature

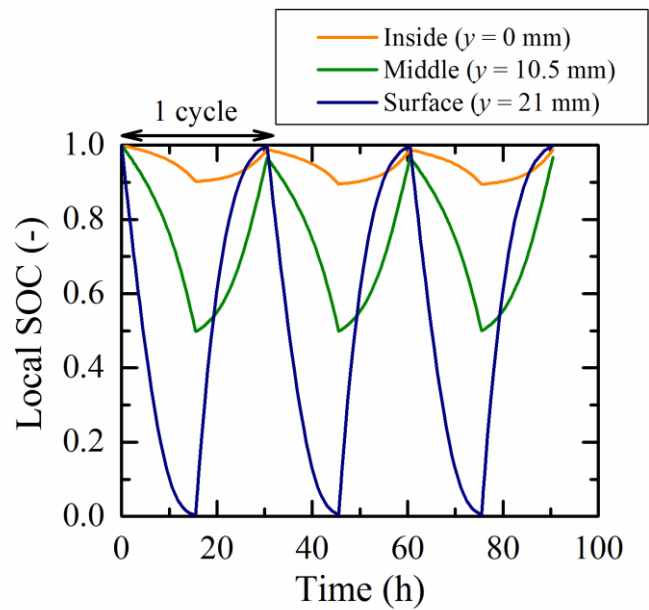


(b) Local SOC

Figure 5.13. Time histories of (a) temperature and (b) local SOC during three-repeated discharge/charge cycle operation with iron density of  $1 \text{ g/cm}^2$ .



(a) Temperature



(b) Local SOC

Figure 5.14. Time histories of (a) temperature and (b) local SOC during three-repeated discharge/charge cycle operation with iron density of  $5 \text{ g/cm}^2$ .

One drawback of this configuration is the nonuniform utilization of the redox metal. Figures 5.13 (b) and 5.14 (b) show the time courses of the local SOC at three positions in the redox metal. When the iron density is  $1 \text{ g/cm}^2$ , as discussed in detail in the above sections, a difference in the local SOC is observed among the three positions. When the iron density is increased to  $5 \text{ g/cm}^2$ , this difference in the local SOC is significantly increased. The SOC of iron near the surface oscillates between 100 and 0%, while that of the inner region always remains above 90%. The iron particles near the surface are subjected to redox cycles involving large changes in SOC that may enhance degradation. As discussed in section 5.2.5, the gas diffusion in the redox metal is reduced particularly at low local SOC region. By enhancing the gas diffusion in the redox metal, e.g. use of pore former etc., difference in the local SOC observed in Fig. 5.14 (b) is expected to be decreased. Careful design is needed to achieve a more uniform reaction of the redox metal.

### 5.3. Summary

A time-dependent 2-D numerical simulation was performed on an SOIAB to reveal the fundamental characteristics of this new system. A simple battery configuration was employed assuming a system with a small capacity. A simulation model for a unit element was developed considering heat and mass transfer in the system, taking both electrochemical and redox reactions into account. Particular attention was paid to the distributions of the local temperature, the concentrations of participating gas species, the reaction rate, the SOC, and the current density of the SOEC.

The numerical results showed the spatial and temporal changes in the temperature field in the charge and discharge operations, which were due to the combined effects of heat generation/absorption by the electrochemical and redox reactions and heat exchange with the air supplied through convective heat transfer. It was found that the system temperature continues increasing during the discharge operation and decreasing during the charge operation under the calculation conditions in this study. This is because the heat generation/absorption by the reactions is greater than the cooling/heating effect due to air convection. As the reaction rates are functions of the local temperature, in this system, thermal management will be a key issue to improve the battery performance. It is possible to maintain the system temperature within a certain range by sequentially operating the battery in the discharge and charge modes since the heat released from the exothermic reactions in the discharge operation can be utilized for the endothermic reactions in the charge operation by using the battery itself as a thermal storage. It was also shown that there is a close relationship between the

current density distribution in the SOEC and the evolution of the active reaction area in the redox metal. The active reaction area proceeds from the surface to the inner region and from upstream to downstream, reflecting the local porosity distribution and the tendency for a high current density in the upstream. This shows that the appropriate gas diffusion is also important for full and effective battery utilization.

## References

- [5.1] R. R. Melkote, K. F. Jensen, Computation of transition and molecular diffusivities in fibrous media, *AIChE J.*, 38 (1992), 56-66.
- [5.2] NIST Chemistry WebBook <http://webbook.nist.gov/chemistry/>.
- [5.3] T. Suzuki, Z. Hasan, Y. Funahashi, T. Yamaguchi, Y. Fujishiro, M. Awano, Impact of Anode Microstructure on Solid Oxide Fuel Cells, *Science*, 325 (2009), 852-855.
- [5.4] T. Kawada, N. Sakai, H. Yokokawa, M. Dokiyo, M. Mori, T. Iwata, Characteristics of Slurry - Coated Nickel Zirconia Cermet Anodes for Solid Oxide Fuel Cells, *J. Electrochem. Soc.*, 137, 3042-3047 (1990).

# Chapter 6

## Conclusions

### 6.1. Conclusions

Numerical analysis of solid oxide iron–air batteries was conducted to understand the heat and mass transfer phenomena inside solid oxide iron–air batteries and to clarify their feasibility mainly from the view points of thermal engineering and/or heat and mass transfer. System round-trip efficiency of a fundamental system configuration was discussed through system analyses while the detailed transport phenomena inside the SOIAB were also investigated. The system round-trip efficiency of the fundamental system with two container configuration assumed in this study is 61% showing the SOIABs' potential as a practical energy storage device. Thermal management is a key to improve of the system round-trip efficiency. The improvement can be achieved by reducing the heat input during the charge operation and/or the heat release during the

discharge operation. The interaction between the electrochemical and redox reactions through the heat and mass transfer was investigated in detail for the single container configuration. The gas diffusion in the porous iron is affected by the change of porous microstructure due to the volume expansion or shrinkage of iron particles during the redox reactions. The increase of diffusion resistance is not catastrophic to deteriorate the battery performance. The iron particles are, however, not uniformly utilized that may enhance degradation of the iron.

The contents of each chapter can be summarized as follows.

Chapter 1 presented the introduction of research on the energy storage systems, the superiority of SOECs and the energy storage systems using SOECs. The research history of SOIAB is also referred.

Chapter 2 presented the outline of the SOIAB system including the reversible reactions at the SOEC and the redox metal during charge/discharge operations, and the classification of the system configurations.

Chapter 3 discussed the system round-trip efficiency and energy flow of the system, based on a 0-D model under a quasi-steady-state assumption. The system round-trip efficiency reaches 61% under the base conditions in this study. The results also show that several limitations exist for the operation parameters and conditions in view of practical applications. In particular, higher and lower limits exist for the fuel and air utilization factors under which the system operates effectively because of constraints such as the maximum allowable fuel-blower temperature and no heat input during the discharge operation.

Chapter 4 presents the study of 1-D analysis of mass transfer effects on the battery. Since the gas transfer between the SOEC and the redox metal is essential to the battery

reactions, the distributions of the participating gas species in the system and their effects on the performance were focused with a simple model. The numerical results for charge/discharge operation qualitatively showed the time-dependent distributions of the related physical quantities such as the gas concentrations, the active reaction region in the redox metal, and its local porosity.

Chapter 5 presents the study of 2-D analysis of both heat and mass transfer effect. Because of heat generation/absorption during the operations, thermal management are dominant factor to the battery performance, in addition to gas transfer effects. The numerical results showed the spatial and temporal changes in the temperature field in the charge and discharge operations, which were due to the combined effects of heat generation/absorption by the electrochemical and redox reactions and heat exchange with the air supplied through convective heat transfer. As the reaction rates are functions of the local temperature, the predicted results show the importance of considering the heat transfer phenomena in this system.

## **6.2. Suggestions for future works**

A simple and small battery model is adopted for a clarification of SOIAB performance throughout this study. The model will increase its practicability with more sophisticated properties and operation control. For example, a dynamic system analysis is important for an efficient and safe operations, as development of a quasi-steady state model assumed in our system round-trip efficiency analysis. It will be helpful to combine our 0-D system analysis in Chapter 3 and 2-D heat transfer analysis in Chapter 5 for more precise prediction of system round-trip efficiency since heat loss will be quantitatively evaluated instead of insulation model assumed in this study. In addition, optimization of porous microstructure of iron and its distribution is another key factor to utilize the battery effectively. While iron particles are assumed to be packed uniformly in our heat and mass transfer analysis, it is useful to reveal optimum packing to decrease the difference in spatial dispersion of the iron utilization.

# Nomenclature

$ASR$	Area-specific resistances of SOEC ( $\Omega \text{ cm}^2$ )
$C_p$	Specific heat ( $\text{J mol}^{-1} \text{ K}^{-1}$ )
$D$	Gas diffusion coefficient ( $\text{m}^2 \text{ s}^{-1}$ )
$E$	Electromotive force of SOEC (V)
$F$	Faraday constant, 96485 ( $\text{C mol}^{-1}$ )
$\Delta G$	Change in Gibbs free energy ( $\text{J mol}^{-1}$ )
$\Delta H$	Enthalpy change ( $\text{J mol}^{-1}$ )
$h$	Heat transfer coefficient ( $\text{W m}^{-2} \text{ K}^{-1}$ )
$i$	Average current density ( $\text{A m}^{-2}$ )
$i_0$	Exchange current density ( $\text{A m}^{-2}$ )
$k$	Reaction coefficient ( $\text{s}^{-1} \text{ Pa}^{-1}$ )
$L$	Length (mm)
$M$	Molar density of reactant ( $\text{mol m}^{-3}$ )
$P$	Electricity input or output (J)
$p$	Average partial pressure (Pa)
$Q$	Heat input or output (J)
$R$	Gas constant, 8.314 ( $\text{J mol}^{-1} \text{ K}^{-1}$ )
$S$	Mass production/consumption ( $\text{mol m}^{-3} \text{ s}^{-1}$ )
$\Delta S$	Entropy change ( $\text{J mol}^{-1} \text{ K}^{-1}$ )
$t$	Process time in hour (h)
$T$	Temperature (K)

$u$	Flow velocity ( $\text{m s}^{-1}$ )
$V$	Terminal voltages (V)
$Y$	Concentration of species ( $\text{mol m}^{-3}$ )

#### Greek symbols

$\varepsilon$	Porosity (-)
$\eta$	System round-trip efficiency (-)
$\eta_C, \eta_D$	Potential losses (V)
$\lambda$	Thermal conductivity ( $\text{W m}^{-1}\cdot\text{K}^{-1}$ )
$\rho$	Mass density ( $\text{kg m}^{-3}$ )
$\tau$	Tortuosity factor (-)

#### Subscripts

$a$	Air
$act$	Activation overpotential loss
$C$	Charge process
$D$	Discharge process
$eff$	Effective value
$IR$	Insulation resistance
$j$	Species
$ohm$	Ohmic loss
$r$	Reaction
$0$	Standard

### Meaning of symbols

EMF	Electromotive force
SOEC	Solid oxide electrochemical cell
SOFC	Solid oxide fuel cell
SOIAB	Solid oxide iron–air battery